

Cosmology with photometric redshift surveys

Chris Blake^{1,2★} and Sarah Bridle^{3★}

¹*Department of Physics & Astronomy, University of British Columbia, 6224 Agricultural Road, Vancouver, BC V6T 1Z1, Canada*

²*School of Physics, University of New South Wales, Sydney, NSW 2052, Australia*

³*Department of Physics & Astronomy, University College London, London, WC1E 6BT*

Accepted 2005 August 15. Received 2005 June 17; in original form 2004 November 26

ABSTRACT

We explore the utility of future photometric redshift imaging surveys for delineating the large-scale structure of the Universe, and assess the resulting constraints on the cosmological model. We perform the following two complementary types of analysis.

(i) We quantify the statistical confidence and the accuracy with which such surveys will be able to detect and measure characteristic features in the clustering power spectrum such as the *acoustic oscillations* and the *turnover*, in a ‘model-independent’ fashion. We show for example that a 10 000-deg² imaging survey with depth $r = 22.5$ and photometric redshift accuracy $\delta z/(1+z) = 0.03$ will detect the acoustic oscillations with 99.9 per cent confidence, measuring the associated preferred cosmological scale with 2 per cent precision. Such a survey will also detect the turnover with 95 per cent confidence, determining the corresponding scale with 20 per cent accuracy.

(ii) By assuming a Λ cold dark matter (Λ CDM) model power spectrum we calculate the confidence with which a non-zero baryon fraction can be deduced from such future galaxy surveys. We quantify ‘wiggle detection’ by calculating the number of standard deviations by which the baryon fraction is measured, after marginalizing over the shape parameter. This is typically a factor of 4 more significant (in terms of number of standard deviations) than the above ‘model-independent’ result.

For both analyses, we quantify the variation of the results with magnitude depth and photometric redshift precision, and discuss the prospects for obtaining the required performance with realistic future surveys. We conclude that the precision with which the clustering pattern may be inferred from future photometric redshift surveys will be competitive with contemporaneous spectroscopic redshift surveys, assuming that systematic effects can be controlled. We find that for equivalent wiggle detection power, a photometric redshift survey requires an area approximately $12[\delta z/(1+z)]/0.03$ times larger than a spectroscopic survey, for a given magnitude limit. We also note that an analysis of luminous red galaxies in the Sloan Digital Sky Survey may yield a marginal detection of acoustic oscillations in the imaging survey, in addition to that recently reported for the spectroscopic component.

Key words: surveys – cosmological parameters – large-scale structure of Universe.

1 INTRODUCTION

Today’s most pressing cosmological questions demand the construction of galaxy surveys of unprecedented depth and volume. Such questions include: is the accelerating rate of cosmic expansion driven by Einstein’s cosmological constant or some different form of ‘dark energy’? What are the properties of this dark energy? Can competing models of inflation be discriminated by accurate measurements of the shape of the primordial power spectrum of mass fluctuations?

Galaxy surveys delineate the large-scale structure of the Universe and thereby provide a powerful and independent constraint on the cosmological model. The currently favoured ‘concordance model’ – in which ≈ 70 per cent of the energy density of today’s Universe is resident in a relatively unclustered form known as ‘dark energy’ – is evidenced by a combination of observations of the cosmic microwave background (CMB) (e.g. Spergel et al. 2003) with either those of galaxy clustering (e.g. Percival et al. 2001) or of high-redshift supernovae (e.g. Riess et al. 1998; Perlmutter et al. 1999). Either pair of these independent data sets is required to break the degeneracies between model parameters and render a unique cosmology.

According to the standard cosmological theory, if the linear-regime clustering power spectrum is measured with sufficient

★E-mail: cab@astro.ubc.ca (CB); sarah@sarahbridle.net (SB)

precision then it will no longer appear smooth and monotonic: specific features and modulations will become apparent. Two such attributes are predicted: first, a series of *acoustic oscillations* – sinusoidal modulations in power as a function of scale imprinted in the baryonic component before recombination (Peebles & Yu 1970; Hu & Sugiyama 1996) – and secondly, a *turnover* – a broad maximum in clustering power on large scales originating from the radiation-dominated epoch. These features encode characteristic cosmological scales that can be extracted from the observations, greatly improving constraints upon cosmological models (e.g. Blake & Glazebrook 2003; Seo & Eisenstein 2003). Moreover, other currently unknown modulations in power (e.g. signatures of inflation) may be discovered when the clustering pattern is examined with sufficiently high precision (e.g. Martin & Ringeval 2004).

Very recently, the acoustic signature has been convincingly identified for the first time in the clustering pattern of luminous red galaxies (LRGs) in the Sloan Digital Sky Survey (SDSS; Eisenstein et al. 2005). The 2dF Galaxy Redshift Survey (2dFGRS) has produced consistent measurements (Cole et al. 2005). These results confirm previous tantalizing hints (e.g. Percival et al. 2001; Miller, Nichol & Chen 2002). The challenge now is to make more accurate measurements at different redshifts, using these features to further constrain the cosmological parameters, in particular the dark energy model. At low redshift, the available volume is limited: the effect of *cosmic variance* is significant. Therefore, such surveys are insensitive to clustering modes on very large scales and are hampered by non-linear growth of structure on small scales. Higher redshift large-scale surveys are consequently required to map greater cosmic volumes: tracing clustering modes with longer wavelengths and additionally unveiling the pattern of linear clustering to significantly smaller scales.

The high-redshift spectroscopic surveys currently being executed [e.g. Deep Extragalactic Evolutionary Probe (DEEP2), Davis et al. 2003; VIMOS VLT Deep Survey (VVDS), Le Fevre et al. 2003] cover solid angles of $\sim 10 \text{ deg}^2$, which are insufficient for detecting the predicted features in the clustering power spectrum. Such projects are fundamentally limited by existing instrumentation, being performed by spectrographs with relatively small fields of view ($\approx 10\text{--}20 \text{ arcmin}$) and restricted (albeit impressive) multi-object capabilities. Some proposed new instrumentation addresses this difficulty [e.g. the Kilo-Aperture Optical Spectrograph (KAOS) project, Barden et al. 2004], permitting spectroscopic exposures over single fields of $\approx 1 \text{ deg}^2$ using ≈ 5000 fibres. However, these projects will take many years to reach completion.

In this paper, we consider the role that *photometric redshift catalogues derived from deep imaging surveys* could play in addressing the scientific goals outlined above. Extensive imaging surveys (covering $\sim 10\,000 \text{ deg}^2$) to reasonable depths ($r \approx 22$) are ongoing (e.g. SDSS); the implied redshift distributions map galaxies over cosmic distances to $z \approx 1$ with sufficient number density that clustering measurements are limited by cosmic variance rather than by shot noise. Future deeper imaging surveys [e.g. Pan-STARRS, Kaiser, Tonry & Luppino 2000; Cerro Tololo Inter-American Observatory (CTIO) Dark Energy Survey (DES), <http://cosmology.astro.uiuc.edu/DES>; Large Synoptic Survey Telescope (LSST), Tyson et al. 2002] are being planned to address a host of scientific questions including in particular weak gravitational lensing. We argue that such surveys will also provide powerful measurements of the features in the galaxy clustering pattern.

The utility of photometric redshifts – derived from broadband galaxy colours rather than from spectra – has been well-established, with many different techniques being successfully utilized. The sim-

plest method involves the fitting of model spectral templates (e.g. Bolzonella, Miralles & Pello 2000). Other approaches use spectroscopic ‘training sets’ to calibrate the photometric redshifts via an empirical polynomial of colour terms (Connolly et al. 1995) or an artificial neural network (Firth, Lahav & Somerville 2003). The precision δz with which galaxy redshifts (and therefore radial distances) may be determined varies with the method and filter set used, together with the galaxy type, magnitude and redshift, but at best is currently $\sigma_0 \equiv \delta z/(1+z) \sim 0.03$ [e.g. Classifying Objects by Medium-Band Observations (COMBO-17), Wolf et al. 2003]. For the SDSS imaging component, the rms photometric redshift accuracy varies from $\delta z \approx 0.03$ for bright galaxies with $r < 18$ to $\delta z \approx 0.1$ for magnitudes $r \approx 21$ (Csabai et al. 2003).

The blurring of large-scale structure in the radial direction due to the photometric redshift error degrades measurements of the clustering pattern. However, *on physical scales larger than that implied by the redshift error, the information is preserved*. Moreover, on smaller scales the tangential information always survives, and the vast area which may be readily covered by an imaging survey can potentially provide more independent structure modes on a given scale than those yielded by a fully spectroscopic survey of a smaller solid angle, implying very competitive cosmological constraints. Photometric redshifts have already been used to construct volume-limited samples of low-redshift galaxies and measure their angular clustering properties (Budavari et al. 2003; see also Meiksin, White & Peacock 1999; Cooray et al. 2001). The cosmological parameter constraints resulting from future photometric redshift imaging surveys have been simulated by Seo & Eisenstein (2003), Amendola et al. (2005) and Dolney, Jain & Takada (2004).

In this study, we use a Monte Carlo approach to model the galaxy power spectra resulting from a host of simulated photometric redshift surveys as a function of the limiting magnitude of the initial imaging and the accuracy of the derived photometric redshift. Our simulation methodology is described in Section 2, where first results for the accuracy of power spectrum measurements are presented. We infer constraints on the cosmological model using two complementary methods with very different prior assumptions. First, in Sections 3 and 4 we discuss in detail the resulting confidence of detection of the acoustic oscillations and power spectrum turnover, respectively, and the accuracy with which the associated characteristic cosmological scales may be extracted. In these analyses, we make minimal assumptions, purely concerning ourselves with the statistical detection of power spectrum features relative to a smooth monotonic fit. Secondly, in Section 5 we use the full power spectrum shape information in conjunction with theoretical fitting formulae to compute constraints on the basic parameters of the cosmological model, in particular the baryon fraction Ω_b/Ω_m and the running of the spectral index of the primordial power spectrum n_{run} . In all cases we compare our results to those deduced from spectroscopic redshift surveys. We evaluate the effect of the approximations of our methodology in Section 6, in particular considering a wider range of photometric redshift error distributions. Finally, in Section 7 we outline the prospects for obtaining the requisite imaging depth and photometric redshift accuracy using realistic future surveys.

2 MODELLING THE POWER SPECTRUM OF PHOTOMETRIC REDSHIFT SURVEYS

2.1 Method summary

Our methodology for simulating the large-scale structure of future galaxy surveys is to generate many ‘Monte Carlo’ realizations of

galaxy distributions from a fiducial power spectrum. An observed power spectrum is measured for each realization separately, using techniques similar to those that would be employed for real survey data. The resulting ensemble of observed power spectra can then be used to quantify the error distribution in derived quantities, without any need to approximate the likelihood surface by techniques such as Fisher matrices (e.g. Seo & Eisenstein 2003; Dolney et al. 2004; Amendola et al. 2005). For example, the standard deviation in the measurement of the power spectrum $P(k)$ in a given bin around scale k follows from the scatter in the recovered values of $P(k)$ in that bin across the realizations, without the need for analytic approximations.

Our procedure for modelling photometric redshifts is to convolve the simulated galaxy distributions in the radial direction with a photometric redshift error function (in the fiducial case, a Gaussian with width σ_x in real space). The measured power spectrum is derived by computing the Fourier transform of the whole survey box, then discarding small-scale radial Fourier modes with wavenumbers $k_{\text{rad}} \gtrsim 1/\sigma_x$ (which contribute no signal due to the radial smearing). Note that the resulting number of useful Fourier structure modes is identical to that obtained if the survey box is instead split into many independent slabs of width σ_x and a purely *angular* power spectrum is measured for each slice.

In particular, we wish to assess the confidence with which we can detect specific features in the clustering power spectrum such as the acoustic oscillations and the ‘turnover’. These features can be modelled by simple empirical formulae, which can be fitted to each measured power spectrum realization, and the best-fitting χ^2 statistic calculated. The resulting best-fitting χ^2 can be compared with that of a smooth (featureless) power spectrum fit, resulting in a *relative probability of feature detection for each realization*. The distribution of the relative probabilities across the Monte Carlo realizations enables a very realistic assessment of the efficacy of future surveys across the statistical ensemble of possible universes.

Furthermore, we are interested in recovering *characteristic scales* from these features in the power spectrum. These scales can be encoded into our empirical fitting formulae; the distribution of best-fitting values of these scales across the realizations is indicative of the realistic accuracy with which it is possible to measure them with the simulated survey.

In order to perform our simulations, we must also adopt a fiducial set of cosmological parameters that determine both the cosmic volume mapped by a given survey and the fiducial power spectrum (via the fitting formulae of Eisenstein & Hu 1998).

We characterize a photometric redshift imaging survey using two parameters.

(i) The photometric redshift error distribution (in the simplest case, a Gaussian distribution with standard deviation δz), which controls the ‘smearing’ of the underlying large-scale structure in the radial direction.

(ii) The threshold apparent magnitude of the input imaging catalogue, m_{lim} , which determines the redshift distribution dN/dz of the ‘unsmeared’ galaxy distribution, i.e. the radial depth of the survey. This magnitude limit is defined using the SDSS r -band filter.

In this paper, we present the results of simulations of a range of photometric redshift surveys as a function of these two parameters. We assume the survey area in all cases is $10\,000\text{ deg}^2$.

In the following section, we provide a detailed account of the assumptions and method we used to simulate the observed power spectra. For analyses of future spectroscopic redshift surveys using a similar method, we refer the reader to Blake & Glazebrook (2003) and Glazebrook & Blake (2005).

2.2 Detailed simulation methodology

(i) A fiducial cosmology is chosen for the simulation. Unless otherwise stated we assumed a flat Λ cold dark matter (Λ CDM) universe with parameters $\Omega_m = 0.3$, $\Omega_\Lambda = 0.7$, $h = 0.7$ and $\Omega_b/\Omega_m = 0.15$.

(ii) A limiting apparent magnitude m_{lim} is assumed for the imaging survey. A model redshift distribution $dN/dz(m_{\text{lim}})$ is determined, as described in Section 2.3.

(iii) A survey redshift range (z_{min} , z_{max}) and solid angle A_Ω is specified. We assumed $A_\Omega = 10\,000\text{ deg}^2$ for our imaging surveys. The chosen redshift interval depends on m_{lim} as described in Section 2.3 (and listed in Table 1).

(iv) We performed our simulations using a ‘flat-sky approximation’ for computational convenience (this approximation has a negligible effect on our results as discussed in Section 6). A cuboid with sides of comoving lengths (L_x , L_y , L_z) is created, possessing a volume equal to that enclosed by the survey cone. We take the x -axis as the radial direction. The length L_x is the comoving distance between redshifts z_{min} and z_{max} , and the other dimensions are determined by stipulating $L_y = L_z$ (although the results are independent of the ratio L_y/L_z , assuming that both of these dimensions are large enough to imply a sensitivity to structural modes with scales contributing to the acoustic oscillations).

(v) A model linear theory matter power spectrum $P_{\text{mass}}(k, z=0)$ is computed for the chosen parameters (Ω_m , Ω_b , h) from the fitting formula of Eisenstein & Hu (1998), assuming a $z=0$ normalization $\sigma_8 = 1$ and a primordial power-law slope $n = 1$. The survey is assumed to have an ‘effective’ redshift $z_{\text{eff}} = (z_{\text{min}} + z_{\text{max}})/2$. The power spectrum is scaled to this redshift using a standard Λ CDM growth factor

$$P_{\text{gal}}(k, z_{\text{eff}}) = P_{\text{mass}}(k, 0) D_1(z_{\text{eff}})^2 b^2, \quad (1)$$

where we use the Carroll, Press & Turner (1992) approximation for $D_1(z)$ and a constant linear bias factor b for the clustering of galaxies with respect to matter. The value $b = 1$ is assumed for our surveys, unless otherwise stated. We neglect any evolution of clustering across the depth of the survey box. This approximation is discussed in Section 6; we note that the clustering amplitude of galaxies is known to evolve much less rapidly with redshift than that

Table 1. Input parameters for simulated galaxy redshift surveys as a function of limiting apparent magnitude in the SDSS r filter, r_{lim} . The ‘unsmeared’ redshift distribution is specified by the values of z_0 and Σ_0 in accordance with equation (6). The minimum and maximum redshifts of the simulated survey, z_{min} and z_{max} , are also listed.

r_{lim}	z_0	$\Sigma_0\text{ (deg}^{-2}\text{)}$	z_{min}	z_{max}
18.0	0.1	120	0.1	0.4
18.5	0.12	230	0.1	0.5
19.0	0.14	410	0.1	0.6
19.5	0.16	710	0.1	0.6
20.0	0.18	1200	0.2	0.7
20.5	0.2	2000	0.2	0.7
21.0	0.22	3200	0.2	0.8
21.5	0.24	4900	0.2	0.8
22.0	0.27	7500	0.2	0.9
22.5	0.3	11 100	0.2	1.0
23.0	0.33	16 300	0.2	1.2
23.5	0.36	24 000	0.2	1.3
24.0	0.39	35 400	0.2	1.4

of the underlying mass fluctuations (indicating an evolution of the galaxy bias parameter in the opposite sense).

(vi) The location in k -space of the transition between the linear and non-linear regimes of gravitational clustering, k_{lin} , is determined from $P_{\text{gal}}(k)$ in a conservative manner (see Blake & Glazebrook 2003, fig. 1). We only measure power spectra in the linear regime, i.e. for scales $k < k_{\text{lin}}$.

(vii) A set of Monte Carlo realizations (numbering 400 for all simulations presented here) is then performed to generate many different galaxy distributions consistent with $P_{\text{gal}}(k)$, as described in steps (viii) and (ix).

(viii) A cuboid of Fourier coefficients is constructed with grid lines set by $dk_i = 2\pi/L_i$, with a Gaussian distribution of amplitudes determined from $P_{\text{gal}}(k)$, and with randomized phases. The gridding is sufficiently fine that the Nyquist frequencies in all directions are significantly greater than k_{lin} .

(ix) The Fourier cuboid is fast Fourier Transformed to determine the density field in the real-space box. The result is modulated by the survey redshift distribution dN/dz . This observed density field is then Poisson sampled to determine the number of galaxies in each grid cell.

(x) A photometric redshift error distribution is assumed. For our main set of simulations, we modelled this function as a Gaussian distribution, such that the radial comoving coordinate x of each galaxy was smeared by an amount δx sampled from a probability distribution

$$f(\delta x) \propto \exp \left[-\frac{1}{2} \left(\frac{\delta x}{\sigma_x} \right)^2 \right]. \quad (2)$$

In practice, we specified a redshift error parameter σ_0 and derived σ_x in accordance with the equation

$$\sigma_x = \delta z \frac{dx}{dz} (z = z_{\text{eff}}) = \sigma_0 (1 + z_{\text{eff}}) \frac{c}{H(z_{\text{eff}})}, \quad (3)$$

where $H(z)$ is the value of the Hubble constant measured by an observer at redshift z . Equation (3) encodes the expected zeroth-order dependence of photometric redshift precision, $\delta z \propto (1 + z)$, originating from the stretching of galaxy spectra with redshift for a filter system with constant spectral resolution $\Delta\lambda/\lambda$. We assess the effect of more complex photometric redshift error distributions than equation (2) in Section 6.1.

(xi) The galaxy number distribution is ‘smeared’ along the x -direction (radial) in accordance with the photometric redshift error function, taking pixelization effects into account. The resulting distribution is our simulated photometric redshift survey. We note that our simple photometric redshift error model represents a convolution of the ‘unsmeared’ galaxy number distribution with the error function $f(x)$ (equation 2). In this case, according to the convolution theorem, the resulting power spectrum signal is damped along the radial direction

$$P(k_x, k_y, k_z) \rightarrow P(k_x, k_y, k_z) \exp \left[- (k_x \sigma_x)^2 \right], \quad (4)$$

where $g(k_x) = \exp[-(k_x \sigma_x)^2]$ is the square of the Fourier transform of $f(x)$.

(xii) The power spectrum of the resulting distribution is measured using standard estimation tools: essentially this involves taking the Fourier transform of the density field, subtracting that of the survey window function and binning up the resulting modes in k -space (see e.g. Hoyle et al. 2002; note that we do not use the optimal weighting technique presented by Feldman, Kaiser & Peacock (1994) because this does not represent a simple convolution of the density field and consequently step (xiii) below would not be possible). Power

spectrum modes in Fourier space are divided into bins of total k , up to a maximum of k_{lin} . We only include modes with a value of $|k_x|$ less than a maximum $k_{x,\text{max}}$. This is because in accordance with equation (4), the photometric redshift smearing damps the clustering signal along the radial direction such that modes with high values of $|k_x|$ contribute only noise. Hence the dominant contribution to power spectrum bins with $k > k_{x,\text{max}}$ originates from tangential Fourier modes with $k_x \approx 0$ and $\sqrt{k_y^2 + k_z^2} \approx k$. The value of $k_{x,\text{max}}$ is determined by the equation

$$k_{x,\text{max}} = 2/\sigma_x, \quad (5)$$

where the coefficient of 2 was determined by experiment to be optimal for the surveys presented here. Use instead of a coefficient of 1.5 does not change the results significantly, but 1 is suboptimal.

(xiii) The measured power spectrum $P(k)$ is ‘undamped’ by dividing by a function $f_{\text{damp}}(k)$. This ‘damping function’ was determined by binning the expression $\exp[-(k_x \sigma_x)^2]$ [from equation (4)] as a function of total k as described in step (xii).

(xiv) An error bar is assigned to each power spectrum bin using the variance measured over the Monte Carlo realizations.

We do not incorporate *redshift-space distortions* into our simulations because the implied radial smearing due to peculiar velocities is much less than that due to the photometric redshift error.

2.3 Modelling the redshift distribution

In order to model the ‘unsmeared’ survey redshift distribution as a function of the limiting apparent magnitude of the imaging survey m_{lim} , we used the luminosity functions derived from the COMBO-17 survey (Wolf et al. 2003). Table A.2 of Wolf et al. (2003) lists Schechter function parameters in redshift slices of width $\Delta z = 0.2$ in the range $0.2 < z < 1.2$ for the SDSS r filter. In the regime $z < 0.2$, we applied the locally determined SDSS luminosity function (Blanton et al. 2003). For a given threshold apparent magnitude r_{lim} , we converted these luminosity functions into a redshift distribution dN/dz for each redshift slice, fitting the overall result with a simple model parametrized by a characteristic redshift z_0 and an overall surface density Σ_0 (in deg^{-2}) (e.g. Baugh & Efstathiou 1993)

$$\frac{dN}{dz} = \Sigma_0 \frac{3z^2}{2z_0^3} \exp \left[- \left(\frac{z}{z_0} \right)^{3/2} \right]. \quad (6)$$

The values of the fitted parameters are displayed in Table 1. We used model K -corrections averaged over different galaxy spectral types.

For each apparent magnitude limit, we selected a redshift interval $(z_{\text{min}}, z_{\text{max}})$ for the simulation. For all but the shallowest surveys we set $z_{\text{min}} = 0.2$, the results are insensitive to this choice because there is minimal volume contained by lower redshifts. As the value of z_{max} increases, the variance in the recovered power spectrum is determined by a balance between two conflicting effects: increasing survey volume (i.e. decreasing cosmic variance) and decreasing average number density (i.e. increasing shot noise) owing to the fixed magnitude threshold. We determined the optimal value of z_{max} for each magnitude threshold by experimenting to determine the most accurate measurement of the acoustic oscillations (see Section 3). Our chosen ranges are listed in Table 1.

We note that the optimal value of z_{max} for measuring power spectrum modes around the turnover is marginally higher than that for detecting the acoustic oscillations, because in the former case the power spectrum amplitude is at a maximum, implying a lower required galaxy number density for suppressing shot noise. We always

use the more conservative values of z_{\max} in Table 1, but this does not change our results significantly.

We note that all magnitudes referred to here are total galaxy magnitudes, and we neglect all incompleteness effects associated with surface brightness. These are expected to be minimal at high redshift owing to the decreasing apparent size of galaxies. We also neglect the fact that imaging surveys to depths $r_{\lim} \gtrsim 23$ may be used to select additional galaxy populations at $z \approx 3$ using the Lyman break technique.

2.4 Fractional errors in the power spectrum

We simulated photometric redshift surveys with limiting magnitudes varying from $r_{\lim} = 20$ to 24 and photometric redshift error parameters in the interval $\sigma_0 = 0.01$ to 0.05. These ranges were chosen to encompass the current state-of-the-art and realistic future improvements. Achieving precision $\sigma_0 = 0.01$ would require observations with many narrow-band filters, probably encompassing the near-infrared.

As a first application of our method, Fig. 1 displays the fractional standard deviation in the power spectrum measurement as a function of scale (averaged over the Monte Carlo realizations) for some example photometric redshift surveys. The measured power spectrum modes are averaged over angles in bins of width $\Delta k = 0.005 h \text{ Mpc}^{-1}$.

The scaling of the resulting power spectrum errors as a function of k can be understood simply by counting the number of Fourier modes, m , within each bin (the errors δP scaling as $1/\sqrt{m}$). For a bin with $k \gg k_{x,\max}$, these modes are located approximately within

an cylindrical annulus in Fourier space of radius k , thickness Δk and depth $k_{x,\max}$. This amounts to a volume in k -space equal to $2\pi k k_{x,\max} \Delta k$, i.e. $\delta P \propto k^{-1/2}$. This contrasts with a fully spectroscopic survey, for which the relevant Fourier modes for a scale k reside within a spherical shell, such that $\delta P \propto k^{-1}$. Although a photometric redshift survey maps out a reduced volume of Fourier space, the larger density of states (owing to the increased cosmic volume probed) can still result in a more accurate measurement of the galaxy power spectrum.

In order to illustrate this point, we compare the power spectrum accuracies for our simulated photometric redshift surveys with those expected for the SDSS spectroscopic surveys (both the main survey and the LRG survey). We created Monte Carlo power spectrum realizations for these SDSS spectroscopic surveys using the methodology of Blake & Glazebrook (2003), which is very similar to that presented in Section 2 above. The main differences are that no photometric redshift smearing is applied, and thus a conical geometry may be employed rather than a flat-sky approximation (although as discussed in Section 6, this makes a negligible difference to the results). We modelled the SDSS main spectroscopic survey using the redshift distribution

$$\frac{dN}{dz} \propto z^2 \exp \left[- \left(\frac{z}{0.055} \right)^{1.31} \right], \quad (7)$$

with a total surface density equal to $\Sigma_0 = 70.7 \text{ deg}^{-2}$. This model constitutes a good fit to the relevant luminosity function (Blanton et al. 2003). The redshift interval of the simulation was $0 < z < 0.25$. We approximated the LRG spectroscopic survey redshift distribution using the Gaussian function

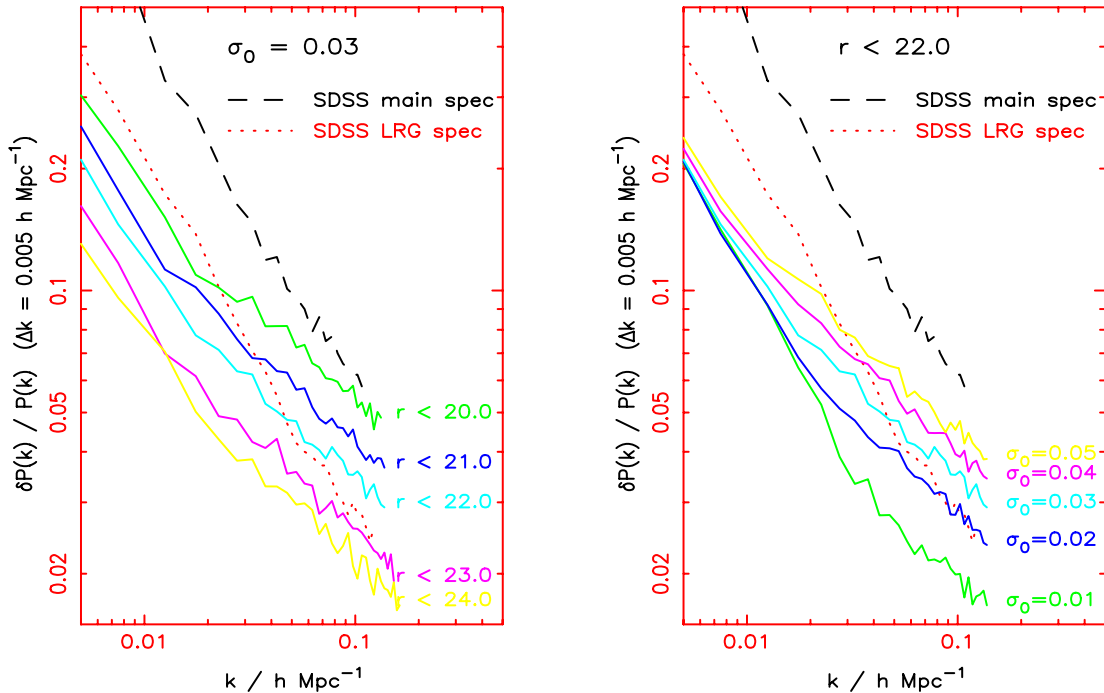


Figure 1. Fractional error in $P(k)$ against k for examples of photometric redshift imaging surveys. The left-hand panel illustrates the variation of the fractional power spectrum error as a function of r_{\lim} for $\sigma_0 = 0.03$; the right-hand panel displays the dependence on σ_0 for $r_{\lim} = 22$. We bin the power spectra in intervals of $\Delta k = 0.005 h \text{ Mpc}^{-1}$. Simulated results for the SDSS main spectroscopic survey (dashed line) and SDSS LRG spectroscopic survey (dotted line) are overplotted (see Section 2.4 for details of our models of these surveys). Considering the photometric redshift surveys, the fractional power spectrum precision improves with increasing survey depth (left-hand panel) owing to the greater cosmic volume mapped and the consequently higher density of states in k -space. The performance degrades with increasing σ_0 (right-hand panel) owing to the decreasing width of the ‘undamped’ slab in k -space (i.e. the decreasing value of $k_{x,\max}$), although on very large scales ($k < k_{x,\max}$) all Fourier modes are retained and performance is unaffected.

$$\frac{dN}{dz} \propto \exp \left[- \left(\frac{z - 0.375}{0.065} \right)^2 \right] \quad (8)$$

and a total surface density $\Sigma_0 = 17.2 \text{ deg}^{-2}$, which provides a reasonable fit to the radial selection function discussed by Eisenstein et al. (2001). The redshift interval of the simulation was $0.3 < z < 0.45$, and LRGs are assigned a linear bias factor $b = 2$ [see equation (1)]. For both spectroscopic surveys we assumed an areal coverage of 10000 deg^2 , the same as for the simulated photometric redshift surveys.

As illustrated by Fig. 1, in the turnover regime ($k < 0.02 h \text{ Mpc}^{-1}$) the photometric redshift surveys always yield more large-scale modes than the SDSS spectroscopic surveys owing to the larger cosmic volume mapped and the fact that the wavelengths of these modes significantly exceed the length-scale of photometric redshift radial smearing. In the acoustic oscillations regime ($k > 0.05 h \text{ Mpc}^{-1}$), a 10000-deg^2 photometric redshift survey outperforms the SDSS LRG spectroscopic survey provided that $\sigma_0 \lesssim 0.03$ and $r_{\text{lim}} \gtrsim 22.5$.

3 MEASURING THE ACOUSTIC OSCILLATIONS USING PHOTOMETRIC REDSHIFT SURVEYS

The clustering power spectrum on intermediate scales ($0.05 < k < 0.3 h \text{ Mpc}^{-1}$) contains small-amplitude (~ 5 per cent) modulations known as ‘acoustic oscillations’ (Peebles & Yu 1970; Hu & Sugiyama 1996; Eisenstein & Hu 1998). These fluctuations in power have an identical physical origin to those observed in the CMB, namely, oscillations in the photon–baryon fluid before recombination.

There has been considerable recent interest in exploiting these acoustic features as an accurate and clean probe of the cosmological model (Blake & Glazebrook 2003; Hu & Haiman 2003; Linder 2003; Seo & Eisenstein 2003). The approximately sinusoidal fluctuations in power encode a characteristic scale – *the sound horizon at recombination* – which can be measured from the CMB. This scale can then act as a *standard cosmological ruler* (Eisenstein, Hu & Tegmark 1999): its recovered value from a galaxy redshift survey depends on the assumed cosmological parameters, in particular the dark energy model, and may be used to constrain those parameters in a manner that is probably significantly less sensitive to systematic error than other probes (Blake & Glazebrook 2003).

Very recently, analysis of the clustering pattern of SDSS LRGs at $z \approx 0.35$ has yielded the first convincing detection of the acoustic signal and application of the standard ruler (Eisenstein et al. 2005). Although this survey does not have sufficient redshift reach to constrain dark energy models, this result is an important validation of the technique. Indeed, *detection of these acoustic features represents a fundamental test of the paradigm of the origin of galaxies in the fluctuations observed in the CMB*.

Utilization of the acoustic oscillations to measure the properties of dark energy demands new galaxy surveys of unprecedented depth and volume (Blake & Glazebrook 2003; Seo & Eisenstein 2003). Given the current availability of large-scale imaging surveys such as the SDSS, and the anticipated wait of several years for commencement of projects with sufficiently capable spectroscopic facilities able to survey $\sim 10^6$ objects over $\sim 1000 \text{ deg}^2$ (such as the KAOS proposal), it is timely to evaluate the role photometric redshift surveys could play in the detection and measurement of the acoustic oscillations. Furthermore, recently developed novel photometric

redshift techniques such as those utilizing *artificial neural networks* should prove extremely useful in this regard (e.g. Collister & Lahav 2004).

The constraints on the cosmological model yielded by acoustic oscillations in future photometric redshift surveys have been discussed by Seo & Eisenstein (2003), Amendola et al. (2005) and Dolney et al. (2004). Here we take a different but complementary approach. First, this previous work deduced cosmological parameter constraints using a Fisher matrix approach that provides the *minimum possible* errors for an unbiased estimate of a given parameter, based upon the curvature of the likelihood surface near the fiducial model. In the present study, we instead use Monte Carlo techniques, which make a closer connection with the analysis methods that would be used for real data and can probe more realistic non-parabolic likelihood surfaces. Secondly, we give detailed consideration to the statistical confidence of detection of the relevant power spectrum features, carefully separating this information from that contained in the overall shape of the power spectrum, which may be subject to additional systematic distortions, as discussed below. Thirdly, by treating a wide grid of potential photometric redshift surveys varying both the redshift accuracy and the limiting magnitude, we can make a direct connection with the performance of current and future experiments.

The comparison of photometric redshift and spectroscopic redshift surveys has already been discussed in detail by Blake & Glazebrook (2003) and Seo & Eisenstein (2003). The relevant points of these two papers are summarized as follows.

(i) As discussed in Section 2.2, Fourier modes with values of $k_x \gg 1/\sigma_x$ (where x is the radial axis) contribute to noise. A photometric redshift survey therefore requires significantly more sky area than a spectroscopic redshift survey of similar depth to yield the same number of Fourier modes in a given power spectrum bin with scale $k \gg 1/\sigma_x$.

(ii) Fourier modes with usable signal-to-noise ratios are largely tangential ($k_x \approx 0$). Consequently, in the case of a photometric redshift survey, we are only able to apply the standard ruler represented by the acoustic oscillations in the tangential direction, constraining the coordinate distance $x(z)$ to the effective redshift of the survey. We lose the capacity of a spectroscopic redshift survey to apply the ruler radially, measuring dx/dz (or equivalently the Hubble constant at redshift z), which yields powerful additional constraints on the dark energy model.

In this section, we present a series of simulations addressing the issues of the *confidence* and *accuracy* of detection of acoustic oscillations as a function of photometric redshift error σ_0 (as defined by equation 2) and limiting apparent magnitude r_{lim} of the imaging survey. We defer the questions of whether and how these requirements can be realized in realistic surveys to Section 7. We proceed in a model-independent fashion, quantifying the statistical significance with which we can assert deviations from a featureless monotonic function, without using any of the information contained in the power spectrum shape. In Section 5, we use a more model-dependent approach, combining the full power spectrum shape function with recent measurements of the CMB anisotropies to derive predicted constraints on the cosmological parameters.

Our set of Monte Carlo realized power spectra enables us to evaluate statistical questions of confidence and accuracy over a realistic ensemble of universes, without needing to approximate the statistical distributions or likelihood surfaces, except that when converting values of the χ^2 statistic to relative probabilities we implicitly assume that the errors in the measured power spectra are Gaussian,

which agrees well with the histograms obtained from the Monte Carlo realizations.

3.1 Confidence of detection of acoustic oscillations

We note that *confidence of detection* can be defined in several different ways and depends strongly on statistical priors. One approach to the data analysis would be to fit full Λ CDM transfer functions (e.g. the formulae of Eisenstein & Hu 1998) to the measured power spectra, and thereby determine that baryonic models (containing acoustic features), provided a significantly better fit to the data than models with $\Omega_b = 0$. We argue in the current section that this only partially constitutes a detection of acoustic oscillations, because information contained in the *shape* of the power spectrum is also constraining this fit.

We adopted a conservative approach in which, prior to measuring the preferred sinusoidal scale, we divided the measured power spectra by a smooth ‘wiggle-free’ reference spectrum. For our purposes, this is the ‘no-wiggles’ spectrum of Eisenstein & Hu (1998) (see also Blake & Glazebrook 2003; with real data, additional smooth polynomial terms can be fitted to remove any residual shape). We therefore do not utilize any information encoded by the shape of the power spectrum. The purpose of our philosophy is to maintain maximum independence from models and systematic effects: the shape of $P(k)$ may be subject to smooth broad-band systematic tilts induced by such effects as complex biasing schemes, a running primordial spectral index and redshift-space distortions. For the acoustic oscillations analysis, the power spectrum is measured in bins of width $\Delta k = 0.01 h \text{ Mpc}^{-1}$. Plots of simulated power spectra divided by reference spectra for different survey configurations are displayed in Fig. 2.

The resulting sinusoidal modulation for each realization is fitted with a simple two-parameter empirical formula describing a decaying sinusoid, i.e. equation (3) from Blake & Glazebrook (2003)

$$\frac{P(k)}{P_{\text{ref}}} = 1 + A k \exp \left[- \left(\frac{k}{0.1 h \text{ Mpc}^{-1}} \right)^{1.4} \right] \sin \left(\frac{2\pi k}{k_A} \right). \quad (9)$$

For each realization, we recorded (i) the best-fitting characteristic scale k_A , (ii) the value of the χ^2 statistic for the ‘no-wiggles’ model [i.e. equation (9) with $A = 0$], $\chi^2_{\text{no-wig}}$ and (iii) the value of the χ^2 statistic for the best-fitting ‘wiggles’ model, $\chi^2_{\text{wig-best}}$. The χ^2 statistic was defined in the usual manner

$$\chi^2 = \sum_i \left[\frac{P_{\text{obs}}(k_i) - P_{\text{model}}(k_i)}{\sigma_P(k_i)} \right]^2. \quad (10)$$

Our flat-sky approximation implies that the off-diagonal terms of the covariance matrix (i.e. correlations between adjacent power spectrum bins) are consistent with zero; this was explicitly tested by computing full covariance matrices for a test case.

A simple relative probability of the ‘no-wiggles’ model and ‘wiggles’ model can be defined by

$$P_{\text{rel}} = \exp \left[- (\chi^2_{\text{no-wig}} - \chi^2_{\text{wig-best}}) / 2 \right] \quad (11)$$

(but see below for further discussion). We note that the distribution of values of P_{rel} across Monte Carlo realizations of the universe is far from symmetric, as illustrated by Fig. 3. In a universe falling at the 50th percentile of the ensemble, the relative probability of the ‘no-wiggles’ model compared to the ‘wiggles’ model would be significantly lower than the mean of the distribution.

As our initial assessment of the confidence of detection of the acoustic oscillations we considered the average value of the quantity

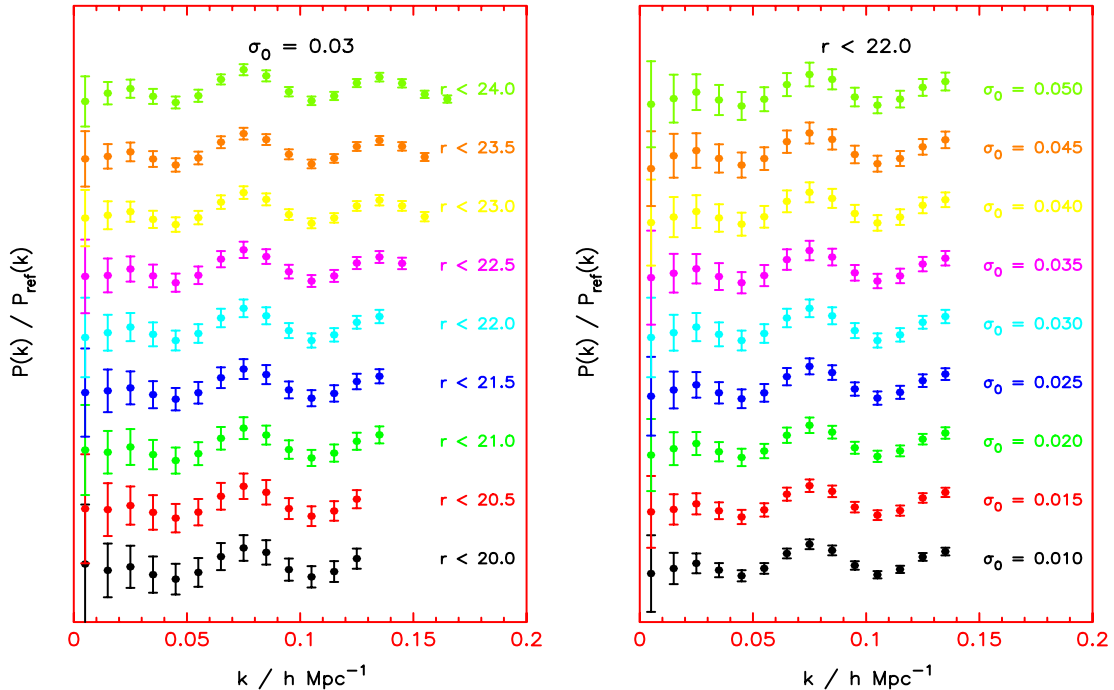


Figure 2. Mean values of the power spectrum divided by the smooth reference spectrum, $P(k)/P_{\text{ref}}$, averaged over the Monte Carlo realizations for various photometric redshift surveys, together with the standard deviation in each bin. The left-hand panel illustrates the variation of the observed $P(k)/P_{\text{ref}}$ as a function of r_{lim} for $\sigma_0 = 0.03$; the right-hand panel displays the dependence on σ_0 for $r_{\text{lim}} = 22$. Results for different surveys are offset for clarity. The power spectra are plotted for wavelengths larger than the linear/non-linear transition scale k_{lin} . This scale varies with the threshold magnitude r_{lim} because it is evaluated at the effective redshift of the survey $z_{\text{eff}} = (z_{\text{min}} + z_{\text{max}})/2$ (see Table 1). In all cases, we use a survey area of $10\,000 \text{ deg}^2$.

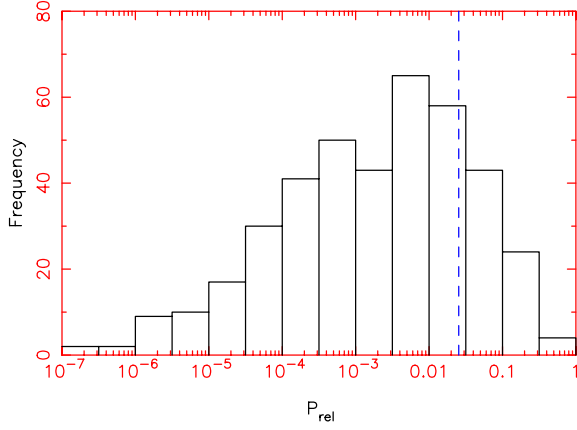


Figure 3. Histogram of values of P_{rel} (defined by equation 11) for 400 Monte Carlo realizations of a survey with $r_{\text{lim}} = 21.5$ and $\sigma_0 = 0.03$, illustrating the skewed distribution of probabilities (note the logarithmic x-axis). The mean value of P_{rel} (as plotted in Fig. 4) is indicated by the vertical dashed line; realizations possess less confident detections of acoustic oscillations than implied by this mean in just 19 per cent of cases.

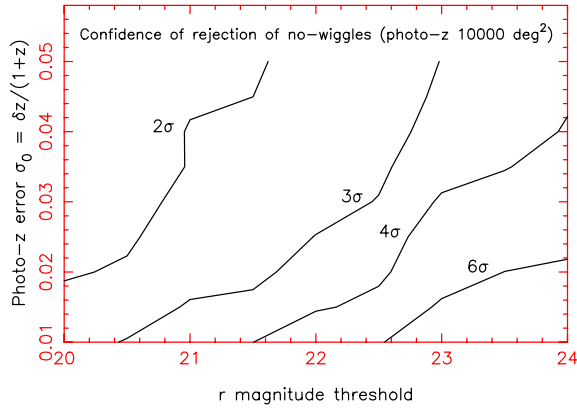


Figure 4. Contours of the detection confidence of acoustic oscillations defined by the average value of $P_{\text{no-wig}} = P_{\text{rel}}/(1 + P_{\text{rel}})$ (equation 11) for photometric redshift imaging surveys with varying magnitude threshold r_{lim} and photometric redshift error parameter σ_0 . The probabilities are expressed as a rejection ‘number of sigmas’ for a Gaussian distribution. We use a survey area of $10\,000 \text{ deg}^2$.

P_{rel} defined by equation (11) over the Monte Carlo realizations. We converted this into a probability for the ‘no-wiggles’ model by using $P_{\text{rel}} = P_{\text{no-wig}}/P_{\text{wig}}$ and $P_{\text{no-wig}} + P_{\text{wig}} = 1$. Contours of $P_{\text{no-wig}}$ (expressed as a rejection ‘number of sigmas’ for a Gaussian distribution) are displayed in Fig. 4 in the parameter space of $(r_{\text{lim}}, \sigma_0)$. In order to obtain a 3σ detection confidence of 99.7 per cent ($P_{\text{no-wig}} = 3 \times 10^{-3}$) we require a survey with parameters such that

$$\sigma_0 \lesssim (r_{\text{lim}} - 19.5)0.01. \quad (12)$$

As an alternative method of quantifying the ‘confidence of detection’ of acoustic oscillations [i.e. the probability that $A \neq 0$ in equation (9)] we considered the following Bayesian approach. We placed a uniform prior on the value of A

$$\begin{aligned} \text{Prior}(A) &= \frac{1}{A_{\text{wid}}} \quad A_{\text{min}} < A < A_{\text{min}} + A_{\text{wid}} \\ &= 0 \quad \text{elsewhere.} \end{aligned} \quad (13)$$

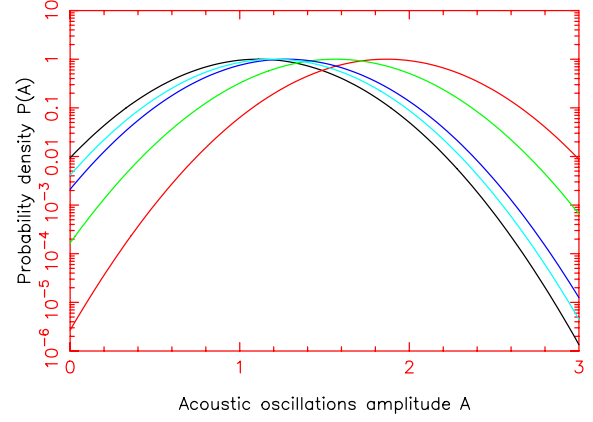


Figure 5. Probability distributions (as defined by equation 14) of amplitude A for the first five Monte Carlo realizations of a survey with parameters $r_{\text{lim}} = 21.5$ and $\sigma_0 = 0.03$. The curves are normalized such that $P(A_{\text{best}}) = 1$. The range of intercepts at $A = 0$ illustrates the distribution of values for $P_{\text{no-wig}}$ across the Monte Carlo realizations.

We chose $A_{\text{min}} = 0$ and $A_{\text{wid}} = 3 \approx 2A_{\Lambda\text{CDM}}$, to be conservative. We assumed prior knowledge of the acoustic wavescale $k_A = 2\pi/s$, where s is the value of the sound horizon at recombination, known very accurately from linear CMB physics [e.g. Eisenstein & Hu (1998), equation (26)]. For an individual power spectrum realization, the probability density as a function of amplitude A is

$$P(A) \propto \exp(-\chi^2/2), \quad (14)$$

where χ^2 is the value of the chi-squared statistic of the fit of equation (9) to the data of that realization (with $k_A = 2\pi/s$). Fig. 5 displays curves of $P(A)$ against A for the first few Monte Carlo realizations of a simulated survey with $r_{\text{lim}} = 21.5$ and $\sigma_0 = 0.03$.

According to Bayesian statistics, the relative probability of a ‘no-wiggles’ and ‘wiggles’ model for one realization is

$$\frac{P_{\text{no-wig}}}{P_{\text{wig}}} = \frac{P(A=0)}{\left[\int_{-\infty}^{\infty} P(A) \text{Prior}(A) dA \right]}. \quad (15)$$

In the numerator of this expression, a δ -function prior centred at $A = 0$ has been integrated over. Fig. 6 plots the average value over

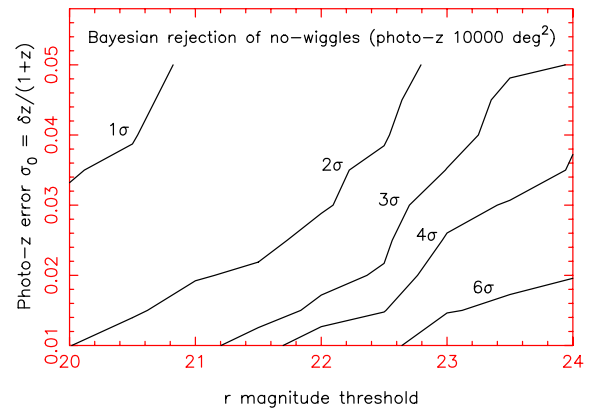


Figure 6. Contours of the detection confidence of acoustic oscillations defined by the average value of the Bayesian quantity $P_{\text{no-wig}}$ (equation 15) for photometric redshift imaging surveys with varying magnitude threshold r_{lim} and photometric redshift error parameter σ_0 . The probabilities are expressed as a rejection ‘number of sigmas’ for a Gaussian distribution. We use a survey area of $10\,000 \text{ deg}^2$.

the Monte Carlo realizations of the quantity $P_{\text{no-wig}}$ defined by equation (15) (expressed as a rejection ‘number of sigmas’ for a Gaussian distribution) in the parameter space of $(r_{\text{lim}}, \sigma_0)$. Note that *less confident* detections of the acoustic oscillations are implied by using this prior, requiring surveys approximately half a magnitude deeper for a 3σ detection. This is reasonable because the probability density of the ‘non-detection’ model with $A = 0$ is being compared to the average probability density of models with $A \neq 0$, rather than only to the best-fitting ‘detection’ model. This serves to illustrate the critical role of priors in quantifying the ‘confidence of detection’. Note that if we had widened our prior yet further by allowing a range in possible model acoustic oscillation scales k_A then an even higher performance survey would be required to achieve the same detection confidence. An alternative prior on the amplitude for the ‘wiggles’ model would have been to use a delta function Prior $(A) = \delta(A - A_{\Lambda\text{CDM}})$, which would produce very similar results to using P_{rel} [of equation (11)].

3.2 Accuracy of measurement of acoustic oscillations

We can also use our simulations to quantify the accuracy with which the characteristic scale (i.e. standard ruler) can be recovered from a photometric redshift survey, as a function of r_{lim} and σ_0 . This is easily obtained as the spread in the best-fitting values of k_A over the Monte Carlo realizations. We defined this spread as half the difference between the 16th and 84th percentiles of the distribution of fitted wavelengths. This quantity is plotted in Fig. 7 as a percentage fractional precision $\Delta k_A/k_A$ in the parameter space of $(r_{\text{lim}}, \sigma_0)$. The precision improves with both increasing r_{lim} and decreasing σ_0 , peaking at ≈ 0.7 per cent for our highest-performance survey ($r_{\text{lim}} = 24$, $\sigma_0 = 0.01$).

In cosmological terms, this precision is equal to the accuracy with which the quantity $x(z_{\text{eff}})/s$ can be determined by the survey (where x is the coordinate distance to the effective redshift of the survey and s is the value of the sound horizon at recombination). This may in turn be converted into confidence distributions for dark energy models (e.g. Seo & Eisenstein 2003; Dolney et al. 2004; Amendola et al. 2005; Glazebrook & Blake 2005).

3.3 Comparison with spectroscopic surveys

It is of great interest to compare the confidence and accuracy of the acoustic oscillation measurement from putative photometric red-

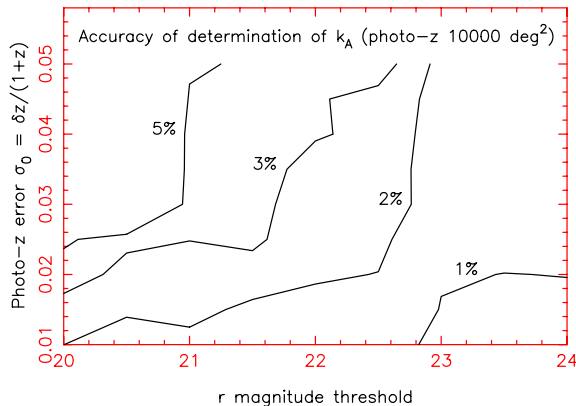


Figure 7. Contours of the accuracy of determination of the characteristic scale k_A for photometric redshift imaging surveys with varying magnitude threshold r_{lim} and photometric redshift error parameter σ_0 . We use a survey area of $10\,000\text{ deg}^2$.

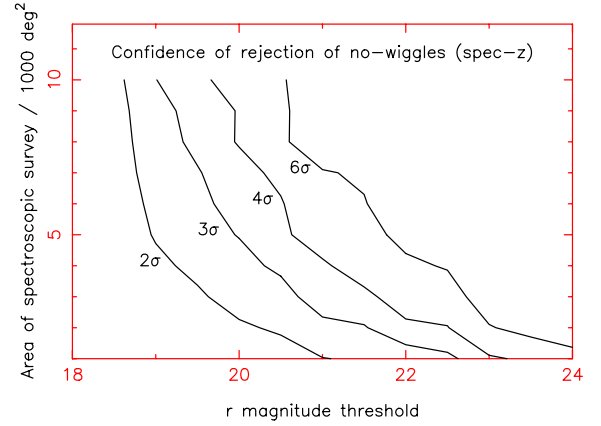


Figure 8. Contours of the detection confidence of acoustic oscillations defined by the average value of $P_{\text{no-wig}} = P_{\text{rel}}/(1 + P_{\text{rel}})$ (equation 11) for spectroscopic redshift surveys with varying magnitude threshold r_{lim} and survey area A_Ω . The probabilities are expressed as a rejection ‘number of sigmas’ for a Gaussian distribution. This plot may be compared directly with Fig. 4 for photometric redshift surveys (note the different ranges of x-axis).

shift surveys with those resulting from future spectroscopic redshift surveys. We therefore created Monte Carlo power spectrum realizations of a grid of spectroscopic surveys, using the same techniques as our photometric survey analysis. We varied the total survey area A_Ω (from 1000 to $10\,000\text{ deg}^2$) and the limiting magnitude threshold r_{lim} (from 18 to 24).

For our spectroscopic survey analyses we assumed the same redshift distributions as a function of r_{lim} listed in Table 1, although we note that a realistic spectroscopic survey would more likely be directed at a subpopulation such as star-forming galaxies with strong emission lines, which would be selected in a more complex manner than a simple magnitude cut.

Our spectroscopic redshift power spectra were analysed for acoustic oscillation measurement in an identical manner to the photometric redshift surveys. For purposes of comparison, we bin power spectra averaging over angles, and do not separate the results into tangential and radial components. Fig. 8 displays the confidence of detection as a function of $(A_\Omega, r_{\text{lim}})$, quantified by the value of $P_{\text{no-wig}}$ in the same manner as Fig. 4. A 3σ detection of the acoustic oscillations can be achieved by a spectroscopic survey with parameters ($A_\Omega = 1000\text{ deg}^2$, $r_{\text{lim}} = 22.5$) or ($A_\Omega = 3000\text{ deg}^2$, $r_{\text{lim}} = 21$). For comparison, an equivalent detection is yielded by a $10\,000\text{-deg}^2$ photometric redshift survey with parameters ($\sigma_0 = 0.05$, $r_{\text{lim}} = 23$) or ($\sigma_0 = 0.01$, $r_{\text{lim}} = 20.5$). Note that the confidences of detection listed here are more conservative (by up to a factor of 4 in terms of the number of standard deviations for a Gaussian distribution) than those which would result from a full fit of a ΛCDM model power spectrum, as discussed and compared in Section 5.1.

Fig. 9 displays the resulting accuracy of measurement of the characteristic acoustic scale; this plot may be compared directly with Fig. 7. For example, a spectroscopic survey of depth $r_{\text{lim}} \approx 22.5$ over $A_\Omega \approx 1000\text{ deg}^2$ will achieve a 2 per cent measurement of the standard ruler (a similar precision is achieved by a $10\,000\text{-deg}^2$ photo-z survey with the same depth and redshift error $\sigma_0 = 0.03$).

Figs 10 and 11 continue the comparison of photometric and spectroscopic surveys. In Fig. 10, we plot the ratio of areas of photometric and spectroscopic surveys achieving the same accuracy of standard ruler measurement for a fixed magnitude threshold common to both surveys. We assume an area of $10\,000\text{ deg}^2$ for the photometric

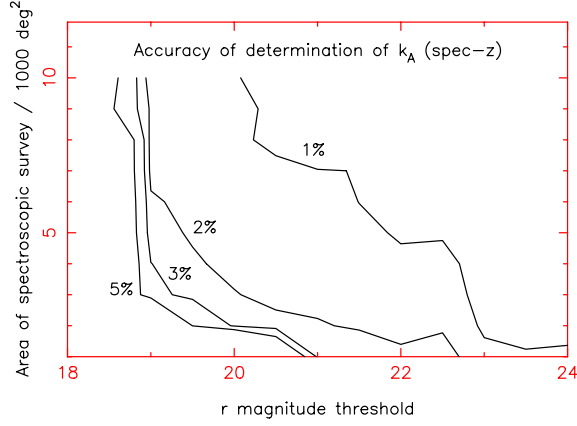


Figure 9. Contours of the accuracy of determination of the characteristic scale k_A for spectroscopic redshift surveys with varying magnitude threshold r_{lim} and survey area A_Ω . This plot may be compared directly with Fig. 7 for photometric redshift surveys (note the different ranges of x -axis).

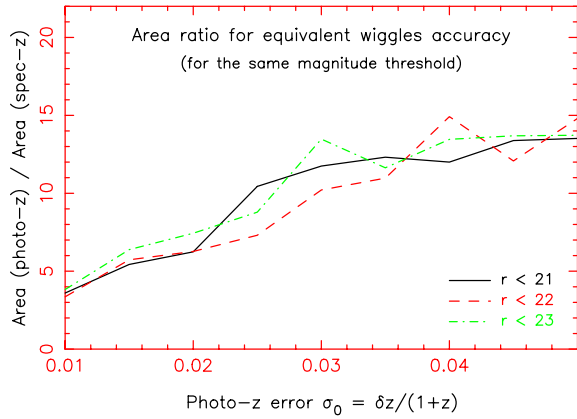


Figure 10. The area ratio of photometric and spectroscopic redshift surveys achieving the same accuracy of standard ruler measurement for a fixed magnitude threshold. This factor is determined by the photometric redshift precision.

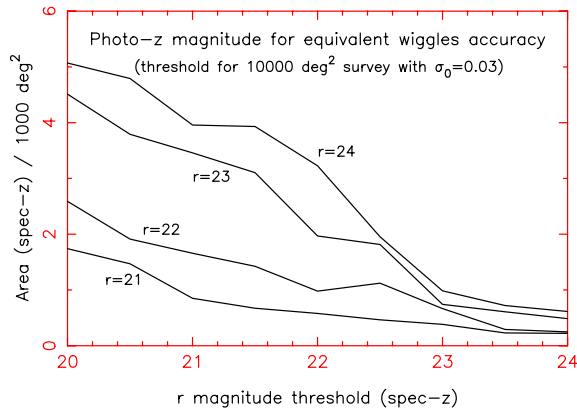


Figure 11. The magnitude threshold required by a 10 000-deg² photometric redshift survey (with $\sigma_0 = 0.03$) to match the standard ruler accuracy of a grid of spectroscopic surveys with varying area and depth.

redshift survey and vary the area of the spectroscopic redshift survey, although the results are expected to apply more generally. From Fig. 10 we see that, for a photometric redshift precision $\sigma_0 = 0.03$, the area ratio for a fixed magnitude threshold is about a factor of

12. This is simply understood by the requirement that the number of Fourier modes contributing to the power spectrum measurement ($m \propto k_{x,\text{max}} A_\Omega \propto A_\Omega / \sigma_0$) must be roughly equal in the two cases. For example, if $\sigma_0 = 0.03$ then $k_{x,\text{max}} \approx 0.02 h \text{ Mpc}^{-1}$. However, for a spectroscopic survey $k_{x,\text{max}} = k_{\text{lin}} \approx 0.2 h \text{ Mpc}^{-1}$, thus the same number of modes m is delivered by a survey area A_Ω reduced by a factor of ≈ 10 . The relation $m \propto A_\Omega / \sigma_0 \approx \text{constant}$ also explains the overall scaling $A_\Omega \propto \sigma_0$ apparent in Fig. 10.

A comparison at common magnitude threshold is of course simplistic: for given observational resources, an imaging survey can readily probe to fainter magnitudes. Therefore, Fig. 11 considers a grid of spectroscopic surveys (parametrized by A_Ω, r_{lim}) and illustrates the magnitude depth required by a 10 000-deg² photometric survey with $\sigma_0 = 0.03$ to match the standard ruler accuracy. The contours ($r_{\text{photo}} = 21 \rightarrow 24$) correspond to standard ruler accuracies in the range 5–1.5 per cent (see Fig. 7).

4 MEASURING THE TURNOVER USING PHOTOMETRIC REDSHIFT SURVEYS

According to standard cosmological theory, the clustering power spectrum should exhibit a ‘turnover’ (i.e. a maximum in power) at a characteristic scale $k_{\text{turn}} \approx 0.015 h \text{ Mpc}^{-1}$. The turnover arises because the primordial power spectrum laid down by cosmological inflation – hypothesized to be a featureless power law $P_{\text{prim}}(k) \propto k^{n_{\text{scalar}}}$, where $n_{\text{scalar}} \approx 1$ – is suppressed by a ‘transfer function’ $T(k)$ owing to radiation pressure in the radiation-dominated epoch. The resulting linear theory power spectrum is derived as $P(k) \propto P_{\text{prim}}(k)T(k)^2$, where $T(k) \approx 1$ for $k < k_{\text{turn}}$ and $T(k)$ decreases towards zero for $k > k_{\text{turn}}$ with an approximate limiting dependence k^{-2} . The characteristic scale k_{turn} is equivalent to the *comoving horizon scale at matter–radiation equality*. This is sensitive to the quantity $\Omega_m h^2$, since the larger the physical density of matter ($\Omega_m h^2$), the earlier matter–radiation equality occurs, and suppression of growth due to radiation oscillations below the Jeans length does not have time to reach larger scales. Therefore, the scale of the turnover is smaller and k_{turn} is larger. (Note that since we measure redshift and not distance, the x -axis of the power spectrum plot is in units of $h \text{ Mpc}^{-1}$, and so the position of the turnover on a plot of $P(k)$ against k/h depends on $\Omega_m h$). Moreover, structure modes with wavelengths larger than the turnover scale are relatively unaffected by physics subsequent to inflation and potentially constitute a probe of the inflationary epoch.

Detection of the turnover in the galaxy clustering pattern constitutes an interesting test of the cosmological paradigm. Its absence may imply either a failure of the standard cosmological theory, or the discovery of new large-scale galaxy biasing mechanisms (e.g. Durrer et al. 2003; i.e. the turnover is more susceptible to systematic distortions than the acoustic oscillations). Successful definition of the turnover requires a survey possessing an extremely large volume to reduce the effect of cosmic variance. In addition, the number density of the tracer galaxies must be sufficient to suppress the shot noise contribution to the power spectrum error. For example, quasi-stellar objects can easily be detected to high redshift but possess an inadequate number density to permit an experiment limited by cosmic variance (Outram et al. 2003). As a result, no survey has clearly measured the turnover yet (in a model-independent manner).

For a turnover detection experiment, spectroscopic-redshift accuracy is not required. The relevant scales are sufficiently large that equivalent information may be recovered from a photometric redshift survey, if the main contribution to the photometric redshift

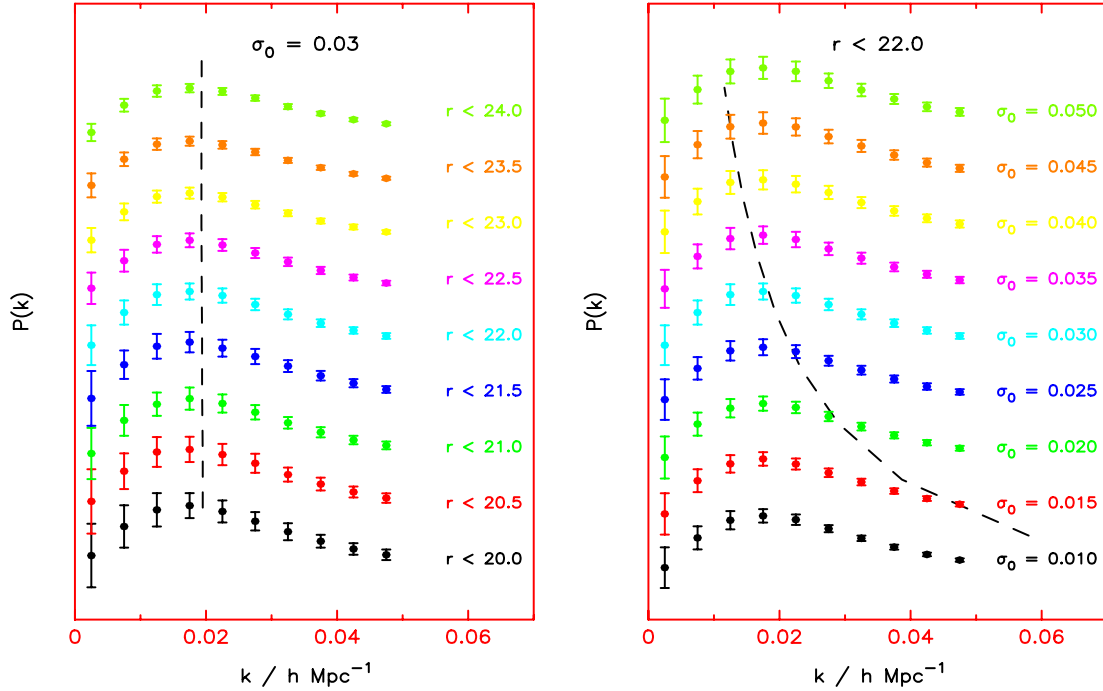


Figure 12. Mean values of the power spectrum $P(k)$ averaged over the Monte Carlo realizations for various surveys, together with the standard deviation in each bin. In this plot we do not divide by any smooth reference power spectrum. The left-hand panel illustrates the variation of the obtained $P(k)$ as a function of r_{lim} for $\sigma_0 = 0.03$; the right-hand panel displays the dependence on σ_0 for $r_{\text{lim}} = 22$. Results for different surveys are offset for clarity. The dashed line tracks the value of $k_{x,\text{max}}$ for the surveys in question. For a bin at $k < k_{x,\text{max}}$, no further improvement in power spectrum precision is possible via more accurate values of σ_0 , rather a survey must go deeper, mapping more cosmic volume and increasing the density of states in k -space. Power spectra are only plotted for scales $k < 0.05 h \text{ Mpc}^{-1}$.

errors is statistical and not systematic. For example, for a survey with $\sigma_0 = 0.03$ and $z_{\text{eff}} = 0.5$, all Fourier modes with $k_x < k_{x,\text{max}} \approx 0.02 h \text{ Mpc}^{-1} > k_{\text{turn}}$ survive the radial damping.

We now consider the detectability of the turnover and implied accuracy of determination of the characteristic scale k_{turn} for a series of simulations varying r_{lim} and σ_0 . As before, our starting point is the ensemble of power spectrum realizations obtained as described in Section 2.2. For the turnover analysis, the power spectrum was measured in bins of width $\Delta k = 0.005 h \text{ Mpc}^{-1}$. Because the turnover in $P(k)$ occurs at an approximate scale of $k_{\text{turn}} \approx 0.015 h \text{ Mpc}^{-1}$, we only utilize power spectrum modes with $k < 0.04 h \text{ Mpc}^{-1}$ (i.e. eight bins). Plots of simulated power spectra for different survey configurations are displayed in Fig. 12.

As with the acoustic oscillations analysis, the significance of detection of the turnover depends on our prior assumptions. We again take a conservative approach, fitting our realized power spectra with a simple empirical parabolic turnover model characterized by four parameters

$$P(k) = P_0 \left[1 - \alpha \left(\frac{k - k_0}{k_0} \right)^2 \right] \quad (k < k_0) \\ = P_0 \left[1 - \beta \left(\frac{k - k_0}{k_0} \right)^2 \right] \quad (k > k_0). \quad (16)$$

The free parameters are the turnover scale k_0 , the maximum of the power spectrum P_0 and the amplitudes of the parabolic decrease of power on either side of the maximum, α and β . In this sense, a detection of the turnover is determined by finding a best-fitting value for α significantly greater than zero, and is governed solely by

power spectrum modes at scales larger than the turnover scale (i.e. $k < k_0$). The requirement that $P(k) \geq 0$ restricts the fitted parameters to lie in the ranges $P_0 \geq 0$, $\alpha \leq 1$, $\beta \leq 1$ and we implement these conditions as strong priors in our fitting process.

By analogy with the acoustic oscillations analysis, we defined the confidence of turnover detection for a given power spectrum realization by comparing the χ^2 statistic for the best-fitting turnover model (i.e. equation 16) with that for the best-fitting ‘no turnover’ model, which we defined as equation (16) with α set equal to zero

$$P_{\text{rel}} = \exp \left[- (\chi_{\text{no-turn}}^2 - \chi_{\text{turn-best}}^2) / 2 \right]. \quad (17)$$

Fig. 13 plots the average value of $P_{\text{no-turn}} = P_{\text{rel}} / (1 + P_{\text{rel}})$ over the Monte Carlo realizations (expressed as a rejection ‘number of sigmas’ for a Gaussian distribution) in the parameter space of $(r_{\text{lim}}, \sigma_0)$. In our highest-performance survey ($r_{\text{lim}} = 24$, $\sigma_0 = 0.01$), the turnover is detected with ≈ 99.5 per cent confidence ($P_{\text{no-turn}} = 0.005$). A 2σ detection in the mean realization requires $r_{\text{lim}} \approx 22.5$. We note that, provided $\sigma_0 \lesssim 0.04$, the detection confidence is independent of the photometric redshift accuracy because all Fourier modes beyond the turnover are retained in our analysis.

Fig. 14 quantifies the accuracy with which the characteristic turnover scale k_{turn} can be recovered from a photometric redshift survey, as a function of r_{lim} and σ_0 , using the same technique as for the characteristic acoustic oscillation scale in Section 3. In the best case we considered, the turnover scale can be measured with a precision of ≈ 12 per cent. This is considerably poorer than the measurement accuracy of the acoustic oscillations scale, owing to the broadness of the turnover and the vastly fewer Fourier modes available at the relevant scales. This observation could in principle yield a 12 per cent measurement of $\Omega_m h$. This in itself is not

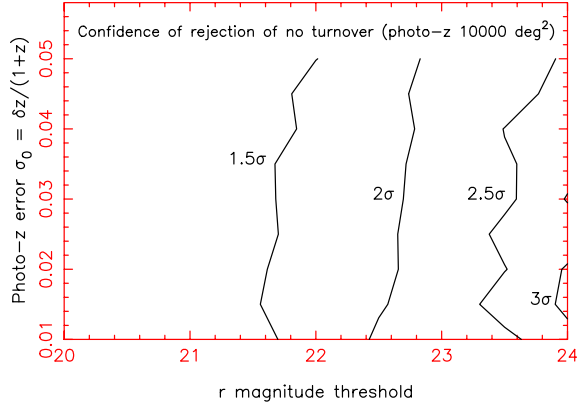


Figure 13. Contours of turnover detection confidence defined by the average value of $P_{\text{no-turn}} = P_{\text{rel}}/(1 + P_{\text{rel}})$ (equation 17) for photometric redshift imaging surveys with varying magnitude threshold r_{lim} and photometric redshift error parameter σ_0 . The probabilities are expressed as a rejection ‘number of sigmas’ for a Gaussian distribution. We use a survey area of 10 000 deg^2 .

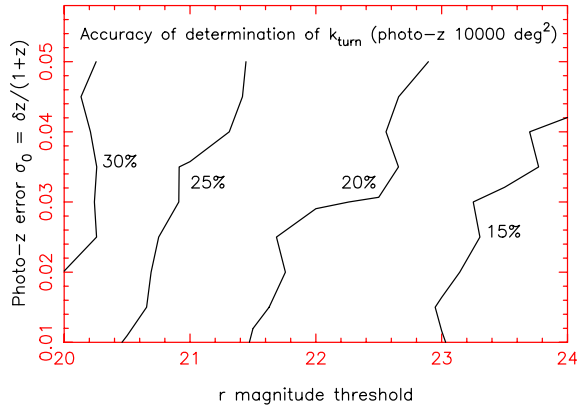


Figure 14. Contours of the accuracy of determination of the characteristic turnover scale k_{turn} for photometric redshift imaging surveys with varying magnitude threshold r_{lim} and photometric redshift error parameter σ_0 . We use a survey area of 10 000 deg^2 .

particularly competitive with other techniques, but performing the analysis in this model-independent way tests the fundamental assumptions made in the standard analyses, and isolates the possible influences of relevant systematic effects. For example, it may indicate that scale-dependent biasing occurs on large scales (e.g. Dekel & Rees 1987), which would constitute a critical observation in the field of galaxy formation. Furthermore, precise measurements of the large-scale clustering pattern may unveil currently unknown signatures of inflation or of non-Gaussianity (e.g. Martin & Ringeval 2004), pointing to a new cosmological paradigm.

Unlike the case of acoustic oscillations measurement, we do not make a comparison with spectroscopic redshift surveys for our turnover detection experiment, because all relevant Fourier modes are retained by a photometric redshift survey, and therefore the results would be unchanged if perfect redshifts were known. Thus, photometric redshift surveys will always be more efficient for turnover detection if the systematic errors can be controlled.

5 MEASUREMENTS OF THE COSMOLOGICAL PARAMETERS

In this section, we adopt a more model-dependent analysis approach to that performed in Sections 3 and 4, assuming the full theoretical framework of ΛCDM transfer functions and calculating how our simulated measurements of the galaxy power spectrum from photometric redshift surveys can be used to constrain cosmological parameters more tightly. Our investigation here is thus independent, but complementary, to the results presented earlier, and indicates how the cosmological conclusions are tightened by the incorporation of more model assumptions.

We assume linear biasing, i.e. the galaxy power spectrum is a constant multiple of the matter power spectrum, and marginalize over this parameter with a flat prior. We assume that the bias parameter does not evolve with redshift, and discuss the effect of this approximation in Section 6.

In order to search parameter space we use Markov Chain Monte Carlo (MCMC) sampling using the Metropolis–Hastings algorithm. In short, an MCMC ‘chain’ is made up of a list of ‘samples’ (coordinates in parameter space) that are obtained from performing trial likelihood evaluations $\text{Pr}(\mathbf{x})$. A new sample at position \mathbf{x}_{i+1} is accepted with a probability $\min[\text{Pr}(\mathbf{x}_{i+1})/\text{Pr}(\mathbf{x}_i), 1]$. The difficulty lies in suggesting good trial positions; we use the latest version of CosmoMC (see Lewis & Bridle 2002 and <http://cosmologist.info/cosmomc> for more information), which uses Code for Anisotropies in the Microwave Background (CAMB; Lewis, Challinor & Lasenby 2000) to calculate CMB and matter power spectra. We ran MCMC chains for the least powerful photometric redshift survey and used importance sampling to find parameter constraints for the better surveys.

We used flat priors on the CMB parameters $\Omega_b h^2$, $\Omega_c h^2$, θ_{peak} , τ , n_s , n_{run} and $\log 10(A_s)$. θ_{peak} is used instead of the Hubble constant h because it renders the MCMC method more efficient when CMB data are included; it is defined by approximate formulae that given the CMB first peak position in terms of the other cosmological parameters. Therefore, for a given set of cosmological parameters, θ_{peak} can be converted into h , and vice versa. For the simulations in this section, we take as our fiducial parameters those from the abstract of Spergel et al. (2003): $h = 0.72$, $\Omega_b h^2 = 0.024$, $\Omega_c h^2 = 0.14$, $\tau = 0.16$, $n_s = 0.99$. The widths of the priors are chosen to be sufficiently large that they have no influence on the results. We assume adiabatic initial conditions with a negligible tensor contribution.

5.1 Measurements of the baryon fraction

First we considered constraints on the baryon fraction resulting from galaxy surveys alone, as a function of $\Omega_m h$. We fixed all other cosmological parameters at their input values for ease of comparison with current galaxy power spectrum analyses (e.g. Cole et al. 2005). We derived results for simulated power spectra from the SDSS main spectroscopic survey (using the survey parameters listed in Section 2.4) and for an SDSS photometric redshift imaging survey (assuming $\sigma_0 = 0.03$, $r_{\text{lim}} = 21$) using a sky area 10 000 deg^2 in both cases. These contours are plotted as the darker lines in Fig. 12. Photometric redshifts from the SDSS imaging survey would produce tighter parameter constraints than the final SDSS spectroscopic survey, if redshift accuracy $\sigma_0 = 0.03$ to a magnitude limit of $r_{\text{lim}} = 21$ could be achieved. This is a challenging requirement, but may be approachable by selecting LRGs.

In order to quantify the contribution of the overall shape to the detection of Ω_b/Ω_m we added in as free parameters the Hubble

constant and the primordial power spectrum tilt parameter n_s . We applied a *Hubble Space Telescope* Key Project (HSTKP) prior on the Hubble constant, otherwise the Hubble constant had significant probability above $100 \text{ km s}^{-1} \text{ Mpc}^{-1}$. The new constraints from the projected SDSS spectroscopic and photometric redshift surveys are shown by the lighter contours in Fig. 12. This is a more rigorous test of detection of acoustic oscillations – hence the slightly wider contours. The effect of relaxing the assumptions on n_s and H_0 is small when the constraints are weak, since the prior that $\Omega_b > 0$ already limits the maximum error bar.

We quantify the constraint on the baryon density by calculating the probability as a function of Ω_b/Ω_m marginalized over $\Omega_m h$ and any other parameters. We then find the error bar by halving the distance between equiprobable limits containing 68 per cent of the probability and quote a ‘number of sigma’ by dividing the fiducial value of Ω_b/Ω_m by this error bar. The ‘number of sigma’ for our full SDSS spectroscopic survey simulation decreases from 3.5 to 2.3 on allowing H_0 to vary within the HSTKP prior and completely freeing the spectral index n_s . For the example photometric redshift survey shown here, it changes from 9 to 5.

We note that the constraints on the baryon density from our analysis are rather weak from the main SDSS survey, despite the fact that it is larger than the full 2dFGRS survey for which the baryon density has already been detected with better confidence. This is because we have assumed a relatively conservative value for the maximum wavenumber fitted by the linear power spectrum, $k_{\text{max}} = 0.11 h \text{ Mpc}^{-1}$ (see Section 2.2). The exact results are quite sensitive to this value. In practice, experimental teams may choose to use a larger value of k_{max} , obtaining tighter contours than those displayed in Fig. 15, but increasing their sensitivity to the systematic uncertainties of modelling the quasi-linear regime. For comparison with existing measurements (e.g. Cole et al. 2005) and for maximum contrast with the ‘model-independent’ sections, we fix H_0 and n_s for the remainder of this section.

Fig. 16 displays how the detection confidence of Ω_b/Ω_m depends on the parameters of a general set of future photometric redshift surveys. We conclude that the significance of measurement of a non-zero value for Ω_b/Ω_m will shortly be greatly improved by the use of photometric redshifts. For a detection with 6σ confidence we require a survey with $r_{\text{lim}} \approx 20$ and $\sigma_0 \lesssim 0.04$.

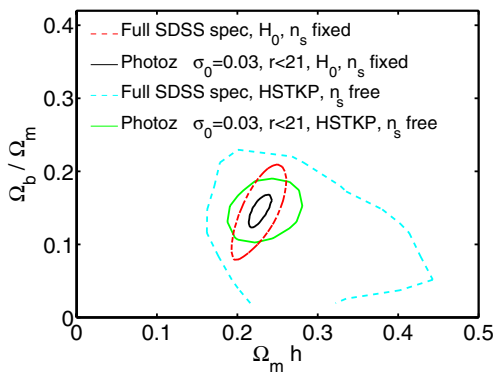


Figure 15. Contours in the parameter space of $(\Omega_b/\Omega_m, \Omega_m h)$ derived from galaxy power spectrum measurements alone. To generate the red and black (darker) lines we fixed other cosmological parameters at their input values. The dashed red (darker) contour is for our projected SDSS spectroscopic survey and the inner solid black (darker) contour is for a photometric survey with $\sigma_0 = 0.03$ and $r < 21$. For the cyan and green (lighter) lines H_0 and n_s are marginalized over using an HSTKP prior of $72 \pm 8 \text{ km s}^{-1} \text{ Mpc}^{-1}$. Only 68 per cent confidence contours are shown, for clarity.

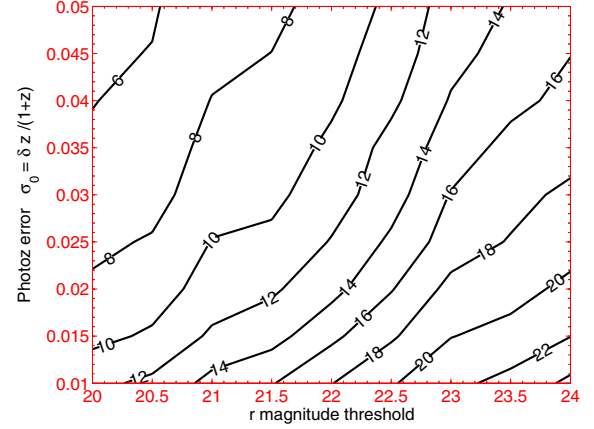


Figure 16. Input value of Ω_b/Ω_m divided by the 68 per cent confidence error margin for Ω_b/Ω_m (loosely speaking, the ‘number of σ of detection’) for a range of photometric redshift surveys with varying magnitude threshold r and photometric redshift error parameter σ_0 . The shape parameter $\Omega_m h$ is varied, as for the darker contours in Fig. 12. We use a survey area of $10\,000 \text{ deg}^2$.

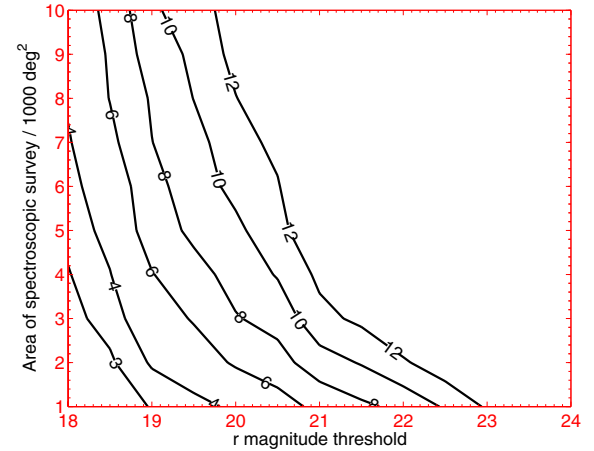


Figure 17. Input value of Ω_b/Ω_m divided by the 68 per cent confidence error margin for Ω_b/Ω_m (loosely speaking, the ‘number of σ of detection’) for a range of spectroscopic redshift surveys with varying magnitude threshold r and area. The shape parameter $\Omega_m h$ is varied, as for the darker contours in Fig. 12.

Equivalent confidences are shown in Fig. 17 for a general set of future deeper spectroscopic redshift surveys. Clearly, for a given magnitude limit, the area required to achieve a detection of $\Omega_b/\Omega_m \neq 0$ is smaller than the $10\,000 \text{ deg}^2$ used for the photometric survey simulations with the same magnitude limit; however, to survey this area is significantly more costly. A quantitative comparison between the results for spectroscopic and photometric redshift surveys is shown in Fig. 18. This is derived from the previous two figures by calculating the area of spectroscopic survey required to obtain the same detection confidence as the $10\,000\text{-deg}^2$ imaging survey, for each magnitude limit and photometric redshift error. From this figure, it can be seen that the factor in area required to make up for the photometric redshift uncertainties is about $12(\sigma_0/0.03)$ and roughly independent of magnitude limit, in good agreement with the ‘model-independent’ analysis.

The value of Ω_b/Ω_m is connected to the presence of the acoustic oscillations in the matter power spectrum, and thus, as discussed

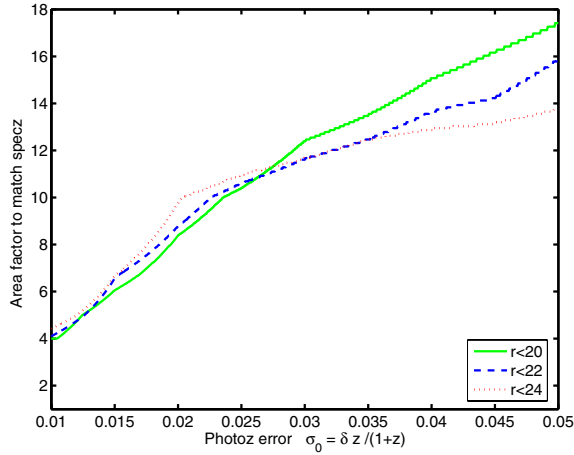


Figure 18. Area factor required to obtain the same accuracy of measurement of Ω_b/Ω_m for a photometric redshift survey as for a spectroscopic survey.

in Section 3, a high-significance measurement of a non-zero value for Ω_b/Ω_m could be considered as a potential ‘detection’ of the existence of these acoustic features. Our treatment in the current section is thus more model dependent than and complementary to our analysis method of Section 3. In the present section, we implicitly assume as a prior the entire Λ CDM framework in which the acoustic oscillation position, amplitude and matter power spectrum shape are intrinsically linked; whereas in Section 3 we adopted a more conservative approach, simply fitting a modified sinusoidal function to the simulated data.

Therefore, it is not surprising that our detection confidences for $\Omega_b/\Omega_m \neq 0$ are somewhat tighter than those for a ‘model-independent’ detection of acoustic oscillations. Roughly, the 8σ lines in Fig. 16 lie on the 2σ lines of Fig. 4. Generally, the number of σ is a factor of 4 larger for the ‘model-dependent’ fit with h and n_s held fixed. As illustrated by Fig. 15, if we instead marginalize over the Hubble constant, with an HSTKP prior and free n_s , then the measurements are much less accurate. The $r < 21$, $\sigma_0 = 0.03$ survey constraint weakens from 9σ to 5σ on freeing h and n_s in this way, compared to 2.2σ for the fully ‘model-independent’ fit.

The two different analysis methods presented in this study (i.e. Sections 3 and 5) are analogous to those used to detect the CMB EE polarization signal [Degree Angular Scale Interferometer (DASI), Kovac et al. 2002; Cosmic Background Imager (CBI), Readhead et al. 2004]. For the first detection of a non-zero signal, the DASI team used a ‘template’ for the shape of the EE power spectrum, taken from the Λ CDM model that best fits the CMB TT data. By contrast, the CBI team were the first to detect the phase and amplitude of the EE polarization signal using a model-independent sine-wave fit, and found that the inferred values were consistent with a Λ CDM model. In order to test the framework of the Λ CDM model we argue that a precise measurement of baryon wiggles in the matter power spectrum using a model-independent fit will be an enormous breakthrough; this being done, more assumptions can then be made to extract the most accurate possible measurements of the cosmological parameters.

5.2 Measurements of the running spectral index

A vital role for measurements of the galaxy power spectrum is to break the parameter degeneracies inherent in the CMB anisotropies. Using a standard six-parameter Λ CDM model, the *WMAP* satellite

measurements can be readily converted to constraints on the matter power spectrum (e.g. Tegmark 2003), which are sometimes erroneously interpreted to mean that there is no need for galaxy redshift surveys. However, the most important current questions in cosmology, such as the quest to quantify the properties of the dark energy and inflation, demand that the simplest cosmological model be extended to encompass additional parameters, such as a time-varying dark energy equation of state and a more general model for the primordial power spectrum of mass fluctuations. In these cases, the degeneracies inherent in the CMB become insuperable, and high-quality additional data are essential.

In the standard six-parameter cosmological model, it is assumed that the scalar perturbations have a power-law power spectrum parametrized by a single spectral index n_s . However, the simplest inflationary models predict that this index should exhibit a slight dependence on scale, often parametrized n_{run} , such that the primordial power spectrum assumes the form

$$P(k) \propto (k/k_0)^{n_s + n_{\text{run}} \log(k/k_0)}, \quad (18)$$

where, according to standard inflationary models, $n_{\text{run}} \sim 0.002$. This parameter n_{run} has been the subject of much recent debate due to the apparent detection of a non-zero value by the *WMAP* team (Spergel et al. 2003) at $n_{\text{run}} = -0.031 \pm 0.024$ from *WMAP*, 2dFGRS, Arcminute Cosmology Bolometer Array Receiver (ACBAR) and CBI. Therefore, we include n_{run} as an additional parameter in our analysis, expanding the total number of fitted parameters to seven (noting that the presence of a running spectral index is potentially degenerate with that of a scale-dependent bias).

Fig. 19 plots the resulting constraints on the primordial power spectrum parameters of equation (18) – n_s and n_{run} – when the *WMAP* CMB data are combined with our simulated 10 000-deg² SDSS main spectroscopic and photometric redshift ($\sigma_0 = 0.03$) surveys. The more accurate power spectrum measurements yielded by the photometric redshift survey helps break the degeneracy between the scalar spectral index n_s and the running spectral index n_{run} [although the exact direction of the degeneracy is determined by the pivot scale in equation (18), for which we use $k_0 = 0.05 \text{ Mpc}^{-1}$].

Fig. 20 displays the (1σ) accuracy of measurement of n_{run} for a general set of future photometric redshift surveys. For comparison, our projection for the full SDSS spectroscopic sample is ± 0.037 . The constraint would be slightly tighter if more CMB data were included in the analysis. The error in n_{run} is halved for our

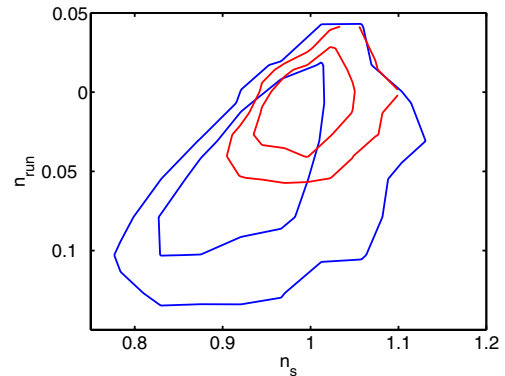


Figure 19. Confidence contours in the parameter space of (n_{run}, n_s) resulting from our simulated SDSS spectroscopic survey (outer contours) and from a simulated SDSS photometric redshift survey with parameters $r_{\text{lim}} = 21$ and $\sigma_0 = 0.03$ (inner contours). In each case, the galaxy power spectrum data is combined with *WMAP* CMB data and we marginalized over the other five cosmological parameters.

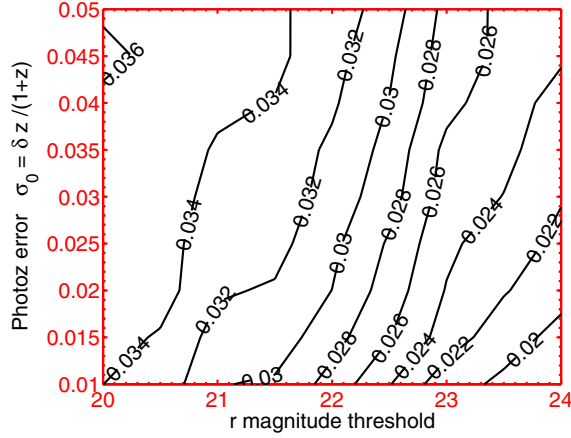


Figure 20. 68 per cent confidence error margin of n_{run} for a range of photometric redshift surveys with varying magnitude threshold r and photometric redshift error parameter σ_0 . In all cases we combined with *WMAP* data and marginalized over the remaining cosmological parameters H_0 , $\Omega_b h^2$, $\Omega_m h^2$, τ , σ_8 and n_s .

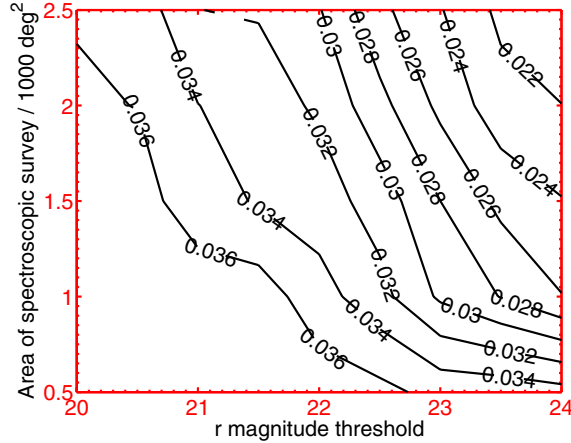


Figure 21. 68 per cent confidence error margin of n_{run} for a range of spectroscopic redshift surveys with varying magnitude threshold r and area. In all cases we combined with *WMAP* data and marginalized over the remaining cosmological parameters H_0 , $\Omega_b h^2$, $\Omega_m h^2$, τ , σ_8 and n_s , as in Fig. 20.

best-possible imaging survey case ($r_{\text{lim}} = 24$, $\sigma_0 = 0.01$), bringing the limit in between that predicted by slow-roll inflation and that indicated by the *WMAP* first-year results.

In Fig. 21, we show the equivalent constraints for a general set of future spectroscopic redshift surveys. We see that to achieve an error bar $\delta n_{\text{run}} = 0.03$, a spectroscopic survey requires about 15 per cent of the area of a photometric redshift survey with $\sigma_0 = 0.03$ to the same magnitude limit.

As discussed above, detection of the matter power spectrum shape on the largest scales is important because it has been unchanged since inflation. In Fig. 22, we indicate the range of model matter power spectra permitted by the *WMAP* data (Hinshaw et al. 2003; Kogut et al. 2003; Verde et al. 2003) plus our fiducial SDSS photometric redshift survey, for a seven-parameter Λ CDM model (i.e. including a free parameter n_{run}). This shows that despite the improvements in power spectrum precision, there is still some freedom in our knowledge of the matter power spectrum on large scales.

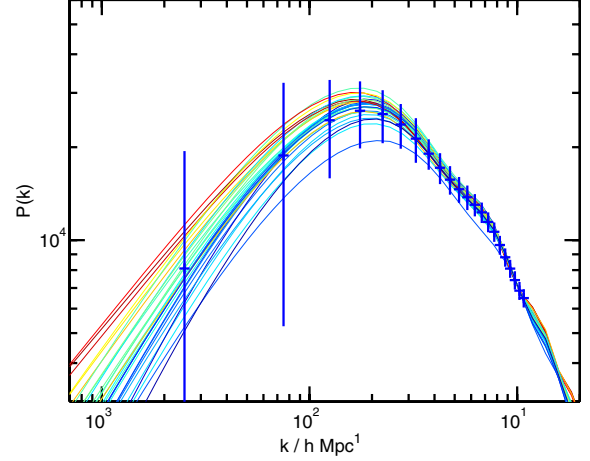


Figure 22. The range of model matter power spectra allowed by the *WMAP* data combined with a photometric redshift survey with parameters $\sigma_0 = 0.03$ and $r < 21$, colour coded according to the value of n_{run} . The plotted data points display the simulated photometric redshift power spectrum. Seven cosmological parameters are allowed to vary: H_0 , $\Omega_b h^2$, $\Omega_m h^2$, τ , σ_8 , n_s and n_{run} . Since we marginalize over the linear bias parameter then for display purposes the power spectra are normalized to go through the highest k data point.

Further relaxations of the post-inflation assumptions will heighten the importance of matter power spectrum information. Whilst the increasing amount of CMB polarization information will help to improve constraints, the range of possible models may be widened even further. For example, in the above we have assumed that the perturbations are adiabatic, with a negligible tensor contribution. Moreover, in addition to adding tensors, a number of isocurvature modes are possible, along with freedom in their spatial correlations (e.g. Bucher et al. 2004). In addition, each mode has a power spectrum that could be relaxed from the power law and gentle running forms assumed here. We would ideally like to reconstruct these power spectra, or equivalently the inflationary potentials. For example a phase transition during inflation can cause a step-like feature in the scalar power spectrum, and trans-Planckian effects can induce ‘ringing’. This additional freedom can be constrained effectively by combining CMB and large-scale structure information (e.g. Bridle et al. 2003; Mukherjee & Wang 2004).

6 ASSESSING OUR APPROXIMATIONS

We now assess the effect of the most significant approximations contained in our methodology for simulating the accuracy of power spectrum measurements (Section 2).

6.1 Photometric redshift error distribution

Our fiducial set of simulations assumed that the statistical distribution of photometric redshift errors could be described by a Gaussian function characterized by a standard deviation (equation 2). This spread can always be measured by obtaining spectra of a complete subsample of the imaged galaxies.

However, a real flux-limited survey will inevitably contain a combination of different classes of galaxy with different intrinsic photometric redshift scatters. For example, LRGs have especially strong spectral breaks which yield improved photometric redshift

precision compared to an average galaxy possessing the same redshift and r -band magnitude.

We assessed the effect of such combinations via several test cases in which the photometric redshift error distribution was modelled by a sum of two Gaussian functions with different widths (denoted σ_1, σ_2) and relative amplitudes (denoted b_1, b_2 such that $b_1 + b_2 = 1$). Specifically, we assumed $\sigma_1 = 0.01$, $\sigma_2 = (0.03, 0.1)$ and $b_2 = (0.1, 0.25)$, such that we are investigating the effect of a *minority subpopulation with a significantly broader error distribution than the majority of galaxies*.

Our motivation is to verify that the single-Gaussian error function in Section 2 does not yield overoptimistic results relative to a more realistic double-Gaussian model with the same standard deviation, i.e. to check that our analysis is conservative. Thus, in each case we compared the fractional power spectrum precision resulting from the double-Gaussian model with that of a single-Gaussian error distribution with the same overall standard deviation ($\sigma_{\text{eff}} = \sqrt{b_1\sigma_1^2 + b_2\sigma_2^2}$).

For the double-Gaussian model, we derived the value of $k_{x,\text{max}}$ in equation (5) by taking the value of σ_x corresponding to the tighter of the two Gaussians (i.e. the dominant galaxy population). We determined by experiment that this was optimal compared to other possible choices, such as σ_x corresponding to the overall standard deviation σ_{eff} .

We found that the precision of power spectrum measurement was never degraded by the assumption of a double-Gaussian model, and in the case ($\sigma_2 = 0.1$, $b_2 = 0.1$) was significantly improved compared to our fiducial predictions for a single-Gaussian model owing to the tighter core of the photometric redshift error distribution. In other words, our previous analysis is indeed conservative: the presence in real survey data of a minority subpopulation of galaxies with significantly poorer photometric redshift precision than the overall standard deviation will not result in poorer power spectrum measurements than those inferred by the equivalent single-Gaussian function.

We also experimented with the addition of an overall systematic offset z_{off} to the mean photometric redshift (relative to the spectroscopic value) of the second of the two Gaussian functions. For the case ($\sigma_2 = 0.03$, $b_2 = 0.1$), the power spectrum precision was degraded by ≈ 10 per cent when $z_{\text{off}} = 0.05$. We note that such systematic effects can always be identified by spectroscopic follow-up of a large enough complete subsample of the imaging survey.

6.2 Bias model

Inference of the clustering pattern from galaxy surveys is always subject to uncertainties associated with the bias model, i.e. the precise manner in which galaxy light traces the underlying mass fluctuations. In our initial simulations, we assumed that this biasing scheme was simply linear; but in general, the bias mechanism will be non-linear, scale-dependent, non-local and evolving with redshift.

Observationally, linear scale-independent bias appears a good approximation for a wide range of galaxy types on the large scales discussed here (e.g. Peacock & Dodds 1994): structure formation is still in the linear regime and the physics of individual galaxy formation should not be relevant. We note however that halo-dependent effects may become important for the most massive galaxies (Peacock & Smith 2000; Seljak 2000).

Even if bias is scale dependent on large scales, it would be very surprising if it induced oscillatory features in k -space liable to obscure the distinctive acoustic peaks and troughs. Our model-

independent analysis of acoustic oscillations detection in Section 3 should be robust to such systematic broadband tilts in the galaxy power spectrum because the overall shape is divided out. Some authors have argued that scale-dependent bias on large scales should obscure the turnover (Durrer et al. 2003); if this property was confirmed observationally then it would undermine our turnover detection analysis of Section 4, but would tell us something interesting about galaxy formation.

In addition, we assume that the biasing scheme does not depend on redshift. This is in conflict with observational data: Lahav et al. (2002) assume a model in which the clustering of galaxies remains constant with time (in comoving space) whilst the dark matter perturbations grow, implying $b(z) = b_0/D(z)$ where $D(z)$ is the linear growth factor. Alternatively, if galaxies are assumed to follow the cosmic flow and remain constant in number then an alternative functional form is produced (Fry 1996) in which the linear bias parameter evolves in proportion to its deviation from unity in the present-day Universe according to $b(z) = 1 + (b_0 - 1)/D(z)$. Our fiducial model is $b(z) = 1$, which is a special case of the Fry equation, and in fitting to the data we have assumed the rather simplistic form $b(z) = b_0$.

We note that despite their differences, all of these models have the same number of free parameters, namely one, b_0 . Therefore, if we were to fit instead the Fry bias model to a simulation with $b(z) = 1$ then we would have the same amount of information available for extracting cosmological parameters. Clearly, $b(z) = 1$ is not a solution of the ‘constant galaxy clustering’ (CGC) model of Lahav et al. (2002), but relative to this model our simulation and detections are conservative, since if $b_0 \sim 1$ today (as measured for the 2dFGRS by Lahav et al. 2002; Verde et al. 2002) and $b(z) = b_0/D(z)$ (CGC model) then the galaxy clustering at higher redshift would be stronger than in our simulation and thus the signal-to-noise ratio available for acoustic oscillation and turnover detection would be increased.

We also point out the following.

- (i) For a power spectrum measurement limited by cosmic variance (such as those discussed here), the fractional error in the power spectrum (e.g. as plotted in Fig. 2) is independent of the overall amplitude of the power spectrum as determined by the bias model.
- (ii) An incorrect assumption about the bias model would not shift the acoustic oscillations along the wavenumber axis; the features would remain in the same place and add up coherently when integrating over redshift.

6.3 Curved-sky effects

Our flat-sky approximation would not be a valid analysis method for a real 10 000-deg² imaging survey: we must either break such a survey into smaller sky areas or utilize a spherical harmonics decomposition along the lines of Percival et al. (2004). However, given that the fractional power spectrum accuracy of our simulated surveys is determined principally by the cosmic volume surveyed, our results should be representative. In order to verify this, we re-analysed the SDSS main spectroscopic survey discussed in Section 2.4 by casting the volume in a flat-sky box rather than a conical geometry (this case is at very low redshift, hence is particularly sensitive to this flat-sky approximation). The resulting power spectrum precision agreed to within 10 per cent.

6.4 Analysis in redshift slices

Application of the flat-sky analysis method to a real photometric redshift survey (with the redshift errors assumed to smear the

distribution along one axis only) must additionally involve the survey being split into redshift slices: any significant ($\gtrsim 20$ per cent) variation of the angular diameter distance across an analysed box would cause a smoothing out of the acoustic features. Again, our results should be representative because, regardless of the number of redshift slices employed, the same number of independent Fourier modes are being utilized (splitting a survey box into N slices decreases the k -space density of states in each slice by a factor of N , but this factor is recovered by averaging over the slices). In order to verify this point, we re-analysed a test case, dividing a broad redshift range into several flat-sky slices such that the volume contained within each slice was equal to the original curved-sky volume (i.e. increasing the width of the flat-sky slice with redshift). We additionally varied the power spectrum amplitude in each slice in accordance with the cosmological growth factor. We obtained the final survey power spectrum by averaging the power spectra measured for the individual slices with inverse-variance weighting. The resulting power spectrum precision (recovered from the Monte Carlo realizations as usual) agreed with our original single-slice analysis to within 5 per cent.

6.5 Angular selection functions

In the present study, we have not considered any effects due to complex angular selection functions, assuming that our survey area is simply a uniform box on the sky. For a more complex survey geometry [e.g. third SDSS data release (DR3)], the observed galaxy power spectrum is smeared out according to the Fourier transform of the observed sky area (and correlations between adjacent power spectrum modes are induced). This convolution will smooth out features such as acoustic oscillations, reducing their detectability, thus surveys with reasonably contiguous geometries are required. For example, the angular selection function of the 2dFGRS (Percival et al. 2001) causes a smearing of the galaxy power spectrum, which is most significant on large scales (i.e. small k) and almost a delta function at $k \sim 0.1 h \text{ Mpc}^{-1}$ (Elgarøy, Gramann & Lahav 2002). Such a selection function would therefore not seriously degrade measurement of the baryon oscillations; detection of the turnover would be largely unaffected if the width of the smearing was smaller than that of the turnover.

6.6 Dust extinction

Extinction by Galactic dust could affect the completeness of a survey with a given magnitude limit, and also compromise the accuracy of the photometric redshifts. This first problem has to be addressed for both spectroscopic and imaging surveys alike, although the greatly increased depth and areas covered by the imaging surveys imply that

this will be a larger problem relative to the small random errors. This issue was discussed in detail by Efstathiou & Moody (2001), and was found to be unimportant for their results but would in general affect the galaxy power spectrum on the largest scales. For the purposes of this paper we have assumed that these effects can be overcome. The second problem affects only the photometric redshift surveys, and addressing this potential problem satisfactorily is beyond the scope of this paper. However, we note that in principle it could be overcome if the photometric redshift algorithm could be calibrated as a function of dust column density, for example, using a number of narrow spectroscopic surveys (training sets) spanning a range of Galactic extinction optical depths.

7 PROSPECTS FOR ONGOING AND FUTURE PHOTOMETRIC REDSHIFT SURVEYS

We now discuss our results in the context of existing or proposed imaging surveys that may be utilized for photometric redshift studies. Table 2 provides a list of such surveys, covering both optical and near-infrared wavebands.

7.1 Photometric redshift estimation techniques

A variety of techniques have been proposed in the literature for derivation of photometric redshifts from multi-colour photometry. The photometric redshift performance depends on the method used, together with a complex combination of the galaxy magnitude and redshift, the filter set, the signal-to-noise ratio of the photometry and the type of galaxy spectrum (in general, redder objects yield more accurate photometric redshifts). A detailed simulation of this myriad of factors is beyond the scope of this paper; however, some general conclusions may be inferred using the photometric redshift accuracies discussed in the literature.

The simplest photometric redshift techniques employ a limited set of ‘template’ spectra corresponding to local elliptical, spiral and starburst galaxies (e.g. Hyper-Z; Bolzonella et al. 2000). These templates may be redshifted and fitted to observed galaxy colours, deriving a likelihood distribution for the galaxy redshift. This approach has been successfully used in many cases (e.g. the Hubble Deep Field North; Fernandez-Soto, Lanzetta & Yahil 1999) and subject to various modifications such as the incorporation of magnitude priors in a Bayesian framework (Benitez 2000) and the iterative improvement of the initial templates (Budavari et al. 2000). Disadvantages of the method include the need for spectrophotometric calibration over a wide wavelength range, the difficulty of incorporating galaxy evolution with redshift and the failure of the template set to encompass all possible classes of observed galaxy.

Table 2. Existing and proposed photometric redshift imaging surveys; we only list projects mapping $\approx 1000 \text{ deg}^2$ or more. For all future surveys the survey parameters are largely illustrative.

Survey	Waveband	Depth	Area (deg^2)	Start date
SDSS DR3	<i>ugriz</i>	$r < 20.8$	5282	Released
UKIDSS	<i>JHK</i>	$K < 18.5$	7500	2005
KIDS	<i>u'g'r'i'z'</i>	$r' < 24.2$	1700	2005
VISTA Wide	<i>YJHK</i>	$K < 19.5, Y < 22.0, J < 21.2, H < 20.0$	3000	2006
VISTA Atlas	<i>JK</i>	$K < 18.2, J < 20.2$	20 000	2006
Pan-STARRS	<i>gRIZY</i>	$R < 27.2$	1200	2008
CTIO DES	<i>griz</i>	$r < 24.1, g < 24.6, i < 24.3, z < 23.9$	5000	2009
VISTA DarkCAM	<i>u'g'r'i'z'</i>	$r \lesssim 25$	$\sim 10\,000$	2009
LSST	<i>rBgiz</i>	$r < 26.5, B < 26.6, g < 26.5, i < 26, z < 25$	15 000	>2012

Table 3. Existing and proposed spectroscopic redshift surveys.

Survey	Selection criteria	Area (deg ²)	No. galaxy redshifts	Status
CFRS	$I_{AB} < 22.5$	~ 0.1	591	Released
CNOC-2	$R < 21.5$	1.5	6200	Released
COMBO17 (Photozs only)	$R < 24$	0.25	10 000	Released
SDSS DR3	$r < 17.1$	4188	374 767	Released
VVDS CDFS (Le Fevre et al. 2004)	$I_{AB} < 24$	$21 \times 21.6 \text{ arcmin}^2$	1599	Released
VVDS Deep	$I_{AB} < 24$	1.3	50 000	Ongoing
VVDS Wide	$I_{AB} < 22.5$	16	100 000	Ongoing
zCosmos	$I_{AB} < 23$	2	90 000	Ongoing
SDSS-2dF LRG	$i < 19.5$ plus colours for $0.4 < z < 0.8$	300	10,000	Ongoing
SDSS LRG	$i < 19.2$ plus colours for $0.15 < z < 0.4$	5000	75 000	Ongoing
SDSS-II	$r < 17.1$	10 000	$\sim 10^6$	Start 2005
DEEP2	$R_{AB} < 24.1$ plus colours for $z > 0.7^1$	3.5	65 000	Ongoing
KAOS	TBD	~ 1000	$\sim 10^6$	Proposed
SKA	TBD	$\sim 30\,000$	$\sim 10^9$	Proposed

¹ Preselected using *BRI* photometry

The availability of a *training set* – spectroscopic redshifts for a complete subsample of imaged galaxies – is very helpful for ‘tuning’ the photometric redshift technique. In Table 3, we list a number of ongoing redshift surveys that could potentially be used for this purpose. In one possible application of the training set, the galaxy redshift is expressed as a polynomial in the colours, and the coefficients are fitted using the training set (Connolly et al. 1995). Further improvements are possible if a different polynomial is adopted in each of a series of cells in colour-space (Csabai et al. 2003). Alternatively, an *artificial neural network* may be trained to deliver similar information (Firth et al. 2003; Collister & Lahav 2004).

7.2 Existing surveys: SDSS

The largest ongoing galaxy survey (Table 2) is the SDSS. Very recently, the *spectroscopic* component mapping LRGs has been utilized to obtain the first convincing detection of the acoustic scale (Eisenstein et al. 2005). The inferred accuracy of the standard ruler in this study was ≈ 4 per cent and the rejection significance of $\Omega_b/\Omega_m = 0$ was 3.4σ . These results agree well with our own simulation (see Section 2.4; we assume an expanded area of $10\,000 \text{ deg}^2$) in which the average value of P_{rel} (equation 11) over the Monte Carlo realizations is 0.035 (i.e. 2.1σ for the ‘model-independent’ method – although 46 per cent of realizations perform better than 3σ – with a full Λ CDM fit expected to improve these figures as noted in Section 5.1). Our simulated standard ruler precision is 2.5 per cent (the difference being explained by a scaling with a survey area of $\sqrt{A_\Omega}$).

Turning now to analyses of the SDSS *imaging* component, Csabai et al. (2003) applied a variety of photometric redshift techniques to the Early Data Release, determining an overall rms redshift scatter $\delta z \approx 0.03$ for $r < 18$, rising to $\delta z \approx 0.1$ at $r \approx 21$, by which point systematic redshift discrepancies due to large photometric errors have become important (i.e. the effective magnitude limit for reliable application of photometric redshifts may be $r_{\text{lim}} \approx 20$). The VVDS survey data bases would constitute a suitable spectroscopic calibration set (see Table 3) for photometric redshift techniques that require it. As discussed in Section 6.1, the inevitable presence of a small fraction of interlopers with significantly larger redshift errors does not compromise the scientific results.

Combining these results with our Figs 4 and 13, we conclude that a photometric redshift analysis of the entire SDSS imaging data base

may not succeed in detecting features in the galaxy power spectrum in the model-independent manner discussed in Sections 3 and 4. For example, even if $\sigma_0 = 0.03$ and $r < 20.5$ were possible, then Figs 4 and 13 would imply a wiggle ‘detection’ with 90 per cent confidence and a turnover ‘detection’ with 80 per cent confidence. However, the prospects for using the Λ CDM fit in Fig. 16 are better, implying a detection of $\Omega_b/\Omega_m \neq 0$ with a significance of 8σ (for fixed values of h and n_s).

However, it is clear that certain subclasses of galaxy perform significantly better regarding photometric redshifts: SDSS red galaxies yield an accuracy twice that of blue galaxies (Csabai et al. 2003), and LRGs permit a rms redshift precision of $\sigma_0 = 0.02$ for $z < 0.55$ (Padmanabhan et al. 2005). In addition, these LRGs inhabit massive dark matter haloes and are consequently biased tracers of the large-scale structure (we assume a linear bias factor $b = 2$). The resulting amplification of the clustering strength implies that a lower space density is required to yield a given power spectrum accuracy, although in some models of galaxy clustering the amplitude of acoustic oscillations is diluted for the most massive galaxies (e.g. Peacock & Smith 2000).

The optimal imaging approach is therefore to analyse an LRG *photometric redshift catalogue* (a suitable spectroscopic training set is the SDSS-2dF LRG redshift survey, see Padmanabhan et al. 2005). We simulated such a catalogue using a redshift interval $0.2 < z < 0.7$, assuming a Gaussian redshift distribution peaking at $z = 0.45$ of standard deviation $z = 0.1$. We supposed LRGs could be selected from the photometric data with a surface density $\Sigma_0 = 100 \text{ deg}^{-2}$ and photometric redshifts measured with an accuracy $\sigma_0 = 0.02$ [i.e. $\delta z = \sigma_0(1 + z_{\text{eff}}) \approx 0.03$; see Padmanabhan et al. 2005]. In addition, LRGs are assigned a linear bias factor $b = 2$. Some of these assumptions may be optimistic, in particular Padmanabhan et al. note that the photometric redshift accuracy degrades for $z > 0.55$. We quantified the confidence of detection of acoustic oscillations for a $10\,000\text{-deg}^2$ survey. The average value of P_{rel} is 0.056, corresponding to a detection slightly less confident than, but comparable to, the LRG spectroscopic data base, with 28 per cent of realizations possessed a ‘model-independent’ confidence exceeding 3σ . The simulated accuracy of the standard ruler measurement is 3.8 per cent. For the turnover analysis, our simulated detection confidence is low: we derive an average value of $P_{\text{rel}} = 0.33$, with an accuracy for the turnover scale of 27 per cent. Again, individual realizations may perform significantly better.

We conclude that the SDSS imaging data set has the potential to yield a marginal model-independent detection of acoustic oscillations using a subsample of red galaxies. However, we caution that the currently available SDSS DR3, which covers a sky area $\approx 5000 \text{ deg}^2$, possesses a complicated angular window function which renders this experiment more difficult: as discussed in Section 6, the observed power spectrum is a convolution of the underlying power spectrum and the survey window function; if this latter possesses a substantial width in Fourier space then the oscillatory signal will be smoothed and consequently harder to detect.

7.3 Future surveys

We now turn our attention to future surveys. We first note that the availability of *near-infrared imaging* to appropriate depths is extremely valuable for galaxies with redshifts $z > 0.4$. In this range, Bolzonella et al. (2000) derived a factor of 2 improvement in redshift accuracy when *JHK* photometry was added to the standard optical wavebands. The combination of the future UKIRT Infrared Deep Sky Survey (UKIDSS) infrared data (see Table 2) with the ongoing SDSS optical survey will therefore be very powerful, and should permit detection of the acoustic oscillations using the complete galaxy population rather than special subclasses. For example, if the photometric error were halved from $\sigma_0 = 0.03$ to $\sigma_0 = 0.015$ (assuming a magnitude threshold $r = 20.5$) then the model-independent wiggle detection limits in Fig. 4 show a detection at 99 per cent confidence (as opposed to just over 90 per cent without the infrared data).

It is clear from Fig. 4 that in order to deliver a *high-significance* measurement of the acoustic peaks using photometric redshifts (together with a significant detection of the power spectrum turnover), a much deeper optical data base is required ($r \sim 24$) over an area of several thousand square degrees. Such a catalogue may first be provided by the CTIO DES (see Table 2). In this case, a photometric redshift precision $\sigma_0 = 0.05$ suffices for delineation of the acoustic oscillations and turnover, a redshift accuracy that has been achieved in existing analyses of the Hubble Deep Field (e.g. Fernandez-Soto et al. 1999). Furthermore, judged solely by the accuracy with which the power spectrum features can be mapped out, this photometric redshift approach will be competitive when compared to the spectroscopic redshift surveys, which will be contemporary to the DES (e.g. the KAOS proposal) – although we note that in terms of measuring the dark energy parameters, a spectroscopic survey yields critical additional information in the radial direction (namely, the Hubble constant at high redshift), which is forfeited by the photometric redshift approach.

The ‘ultimate’ photometric redshift survey would cover an area A_Ω , approximating the whole sky to a magnitude depth $r \sim 26$; surveys with the LSST will approach these specifications (see Table 2). If we assume that the redshift accuracy cannot exceed the limit $\sigma_0 = 0.01$, in this best case a competing spectroscopic survey would need to cover $A_\Omega/4 \sim 10\,000 \text{ deg}^2$ to produce comparable power spectrum constraints (i.e. trace the same number of Fourier structure modes). In optical wavebands, spectrographs with fields of view greatly exceeding 1 deg^2 are prohibitively expensive, but we note that redshift surveys for neutral hydrogen using a next-generation radio telescope such as the Square Kilometre Array would become competitive here (Blake et al. 2004), provided that such a telescope was designed with an instantaneous field of view of order 100 deg^2 at frequency 1.4 GHz.

We note that ultimately the matter power spectrum derived from gravitational lensing will circumvent the assumptions about bias

necessary for the interpretation of galaxy surveys. Of course, lensing investigations can be performed with the identical imaging data sets discussed here, and indeed the application of photometric redshifts will form an important part of that interpretation. However, due to the unknown intrinsic shapes of galaxies, many galaxies have to be averaged to obtain a cosmic shear signal. Therefore, we will always be able to obtain constraints from the galaxy power spectrum that are vastly tighter than those inferred from the lensing power spectrum, albeit less reliable owing to the caveats regarding bias. Thus, galaxy surveys are the best place to look for the first glimpses of any exciting new physics revealed by studies of large-scale structure.

8 CONCLUSIONS

We have used Monte Carlo techniques to estimate the measurement precision of the galaxy power spectrum achievable using photometric redshift imaging surveys with a variety of magnitude depths and photometric redshift accuracies. We have focussed on two main areas.

(i) The ‘model-independent’ measurement of specific features in the galaxy power spectrum: the acoustic oscillations and the turnover. In particular, we have carefully quantified the statistical confidence with which these features may be detected, together with the accuracy with which the acoustic and turnover scales can be inferred.

(ii) The assumption of the Λ CDM paradigm to place tighter constraints on the baryon fraction Ω_b/Ω_m from galaxy surveys alone, and an evaluation of the additional constraints on the running of the spectral index of the primordial power spectrum as increasingly powerful galaxy surveys are combined with *WMAP*.

We summarize our general findings as follows.

(i) On linear-regime scales, a large photometric redshift survey can provide competitive power spectrum measurements when compared to contemporaneous spectroscopic surveys. For example, given a magnitude threshold $r_{\text{lim}} = 23$, a $10\,000\text{-deg}^2$ photometric redshift survey with error parameter $\sigma_0 = 0.03$ results in a confidence of detecting the acoustic oscillations that is comparable to a spectroscopic survey covering 1000 deg^2 . (Albeit with the loss of radial information that is helpful for constraining dark energy models).

(ii) We compare various different definitions of ‘detection of acoustic oscillations’, the most optimistic of which is a Λ CDM fit to the data (i.e. derivation of a baryon fraction significantly exceeding zero), which (for fixed values of h and n_s) yields detections with statistical significance approximately a factor of four σ ’s greater than our default ‘model-independent’ fit using no shape information.

(iii) Concerning the power spectrum turnover, the relevant scales are sufficiently large that photometric redshifts with precision better than $\sigma_0 = 0.04$ retain information equivalent to spectroscopic surveys. An imaging depth $r \sim 24$ is required to deliver a 3σ detection confidence.

(iv) Our results are robust against more complex photometric redshift error distributions such as double-Gaussian models, if our parameter σ_0 is interpreted as the overall rms error.

In terms of realistic ongoing and future surveys we have the following.

(i) The SDSS has already yielded a convincing detection of acoustic features in the spectroscopic survey of LRGs. A marginal ‘model-independent’ detection may also follow from this sample.

(ii) Analysis of an LRG photometric redshift data base selected directly from the imaging data may yield a measurement of comparable precision.

(iii) Assuming a Λ CDM model and calculating the number of standard deviations by which Ω_b/Ω_m (marginalized over the shape parameter $\Omega_m h$) exceeds zero shows that, for our simulated full SDSS spectroscopic survey the baryons would be detected at 3.5σ , whereas for a photometric redshift survey to magnitude depth $r < 21$ with $\delta z = 0.03(1+z)$ the detection level is 9σ . We note that these analyses assume a conservative specification of the maximum wavenumber, k_{\max} , for which a linear power spectrum is fitted.

(iv) A high-significance analysis of the acoustic oscillations from photometric redshifts, and a model-independent detection of the power spectrum ‘turnover’, requires a significantly deeper optical data base ($r \sim 24$) over an area of several thousand square degrees.

ACKNOWLEDGMENTS

CB acknowledges Karl Glazebrook for an invaluable collaboration developing simulations of experiments measuring the wiggles, and for useful comments on a draft of this paper. CB is also grateful to the Australian Research Council for financial support, and acknowledges current funding from the Izaak Walton Killam Memorial Fund for Advanced Studies and the Canadian Institute for Theoretical Astrophysics. We thank Adrian Collister, George Efstathiou, Ofer Lahav and David Woods for helpful comments. SLB thanks the Royal Society for support in the form of a university research fellowship. SB thanks Antony Lewis for various improvements to COSMOMC. COSMOMC calculations were performed on the UK National Cosmology Supercomputer Centre funded by PPARC, HEFCE and Silicon Graphics/Cray Research. We thank Andy Taylor and Konrad Kuijken for advising on the VISTA DarkCAM and KIDS planned survey parameters, respectively. We thank Berkeley for hospitality while this work was being finished.

REFERENCES

- Amendola L., Quercellini C., Giallongo E., 2005, *MNRAS*, 357, 429
- Barden S. C., Dey A., Boyle B. J., Glazebrook K., 2004, in Moorwood A., Iye N., eds, *Proc. SPIE 5492, Ground-Based Instrumentation for Astronomy*. SPIE, Bellingham
- Baugh C. M., Efstathiou G., 1993, *MNRAS*, 265, 145
- Benítez N., 2000, *ApJ*, 536, 571
- Blake C. A., Glazebrook K., 2003, *ApJ*, 594, 665
- Blake C. A., Abdalla F., Bridle S. L., Rawlings S., 2004, *New Astron. Rev.*, 48, 1063
- Blanton M. R. et al., 2003, *ApJ*, 592, 819
- Bolzonella M., Miralles J.-M., Pello R., 2000, *A&A*, 363, 476
- Bridle S. L., Lewis A. M., Weller J., Efstathiou G. P., 2003, *MNRAS*, 342, 72
- Bucher M., Dunkley J., Ferreira P. G., Moodley K., Skordis C., 2004, *Phys. Rev. Lett.*, 93, 1301
- Budavari T., Szalay A. S., Connolly A. J., Csabai I., Dickinson M., 2000, *AJ*, 120, 1588
- Budavari T. et al., 2003, *ApJ*, 595, 59
- Carroll S. M., Press W. H., Turner E. L., 1992, *ARA&A*, 30, 499
- Cole S. et al., 2005, *MNRAS*, 362, 505
- Colless M. et al., 2001, *MNRAS*, 328, 1039
- Collister A., Lahav O., 2004, *PASP*, 116, 345
- Connolly A. J., Csabai I., Szalay A. S., Koo D. C., Kron R. G., Munn J. A., 1995, *AJ*, 110, 2655
- Cooray A., Hu W., Huterer D., Joffe M., 2001, *ApJ*, 557, 7
- Csabai I. et al., 2003, *AJ*, 125, 580
- Davis M. et al., 2003, *Proc. SPIE*, 4834, 161
- Dekel A., Rees M. J., 1987, *Nat*, 326, 455
- Dolney D., Jain B., Takada M., 2004, *MNRAS*, 352, 1019
- Durrer R., Gabrielli A., Joyce M., Sylos Labini F., 2003, *ApJ*, 585, 1
- Eisenstein D. J., Hu W., 1998, *ApJ*, 496, 605
- Eisenstein D. J., Hu W., Tegmark M., 1999, *ApJ*, 518, 2
- Eisenstein D. J. et al., 2001, *AJ*, 122, 2267
- Eisenstein D. J. et al., 2005, *ApJ*, in press (astro-ph/0501171)
- Elgarøy Ø., Gramann M., Lahav O., 2002, *MNRAS*, 333, 93
- Efstathiou G., Moody S., 2001, *MNRAS*, 325, 1603
- Feldman H. A., Kaiser N., Peacock J. A., 1994, *ApJ*, 426, 23
- Fernandez-Soto A., Lanzetta K. M., Yahil A., 1999, *ApJ*, 513, 34
- Firth A. E., Lahav O., Somerville R. S., 2003, *MNRAS*, 339, 1195
- Freedman W. et al., 2001, *ApJ*, 553, 47
- Fry J. N., 1996, *ApJ*, 461, 65
- Glazebrook K., Blake C., 2005, *ApJ*, in press (astro-ph/0505608)
- Hinshaw G. et al., 2003, *ApJ*, 148, 135
- Hoyle F., Outram P. J., Shanks T., Croom S. M., Boyle B. J., Loaring N. S., Miller L., Smith R. J., 2002, *MNRAS*, 329, 336
- Hu W., Haiman Z., 2003, *Phys. Rev. D*, 68, 063004
- Hu W., Sugiyama N., 1996, *ApJ*, 471, 542
- Kaiser N., Tonry J. L., Luppino G. A., 2000, *PASP*, 112, 768
- Kovac J. et al., 2002, *Nat*, 420, 772
- Kogut A. et al., 2003, *ApJ*, 148, 161
- Lahav O. et al., 2002, *MNRAS*, 333, 961
- Le Fevre O. et al., 2003, *Proc. SPIE*, 4834, 173
- Le Fevre O. et al., 2004, *A&A*, 428, 1043
- Lewis A., Bridle S. L., 2002, *Phys. Rev. D*, 66, 3511
- Lewis A., Challinor A., Lasenby A., 2000, *ApJ*, 538, 473
- Linder E. V., 2003, *Phys. Rev. D*, 68, 083504
- Martin J., Ringeval C., 2004, *Phys. Rev. D*, 69, 83515
- Meiksin A., White M., Peacock J. A., 1999, *MNRAS*, 304, 851
- Miller C. J., Nichol R. C., Chen X., 2002, *ApJ*, 579, 483
- Mukherjee P., Wang Y., 2004, *ApJ*, 613, 51
- Outram P. J., Hoyle F., Shanks T., Croom S. M., Boyle B. J., Miller L., Smith R. J., Myers A. D., 2003, *MNRAS*, 342, 483
- Padmanabhan N. et al., 2005, *MNRAS*, 359, 237
- Peacock J. A., Dodds S. J., 1994, *MNRAS*, 267, 1020
- Peacock J. A., Smith R. E., 2000, *MNRAS*, 318, 1144
- Peebles P. J. E., Yu J. T., 1970, *ApJ*, 162, 815
- Percival W. J. et al., 2001, *MNRAS*, 327, 1297
- Percival W. J. et al., 2004, *MNRAS*, 353, 1201
- Perlmutter S. et al., 1999, *ApJ*, 517, 565
- Readhead A. et al., 2004, *Sci*, 306, 836
- Riess A. G. et al., 1998, *AJ*, 116, 1009
- Seljak U., 2000, *MNRAS*, 318, 203
- Seo H., Eisenstein D. J., 2003, *ApJ*, 598, 720
- Spergel D. N. et al., 2003, *ApJS*, 148, 175
- Tegmark M., 2003, in Holt S. S., Reynolds C. S., eds, *AIP Conf. Proc. Vol. 666, The Emergence of Cosmic Structure: Thirteenth Astrophysics Conference*. Am. Inst. Phys., New York, p. 19
- Tyson J. A. et al., 2002, *Proc. SPIE*, 4836, 10
- Verde L. et al., 2002, *MNRAS*, 335, 432
- Verde L. et al., 2003, *ApJS*, 148, 195
- Wolf C., Meisenheimer K., Rix H.-W., Borch A., Dye S., Kleinheinrich M., 2003, *A&A*, 401, 73
- York D. G. et al., 2000, *AJ*, 120, 1579

This paper has been typeset from a $\text{\TeX}/\text{\LaTeX}$ file prepared by the author.